The wobbly Galaxy: kinematics north and south with RAVE red-clump giants

M. E. K. Williams,[1]⋆ M. Steinmetz,[1] J. Binney,[2] A. Siebert,[3] H. Enke,[1] B. Famaey,[3] I. Minchev,[1] R. S. de Jong,[1] C. Boeche,[4] K. C. Freeman,[5] O. Bienaymé,[3] J. Bland-Hawthorn,[6] B. K. Gibson,[7] G. F. Gilmore,[8] E. K. Grebel,[4] A. Helmi,[9] G. Kordopatis,[8] U. Munari,[10] J. F. Navarro,[11]† Q. A. Parker,[12] W. Reid,[12] G. M. Seabroke,[13] S. Sharma,[6] A. Siviero,[1,14] F. G. Watson,[15] R. F. G. Wyse[16] and T. Zwitter[17]

[1]*Leibniz Institut für Astrophysik Potsdam (AIP), An der Sterwarte 16, D-14482 Potsdam, Germany*
[2]*Rudolf Pierls Center for Theoretical Physics, University of Oxford, 1 Keble Road, Oxford OX1 3NP, UK*
[3]*Observatoire Astronomique, Université de Strasbourg, CNRS, 11 rue de l' université, F-67000, Strasbourg, France*
[4]*Astronomisches Rechen-Institut, Zentrum für Astronomie der Universität Heidelberg, D-69120 Heidelberg, Germany*
[5]*Mount Stromlo Observatory, RSAA Australian National University, Cotter Road, Weston Creek, Canberra, ACT 72611, Australia*
[6]*Sydney Institute for Astronomy, School of Physics, University of Sydney, NSW 2006, Australia*
[7]*Jeremiah Horrocks Institute for Astrophysics & Super-computing, University of Central Lancashire, Preston PR1 2HE, UK*
[8]*Institute of Astronomy, University of Cambridge, Madingley Road, Cambridge CB3 0HA, UK*
[9]*Kapteyn Astronomical Institute, University of Groningen, Postbus 800, NL-9700 AV Groningen, the Netherlands*
[10]*INAF – Astronomical Observatory of Padova, I-36012 Asiago (VI), Italy*
[11]*University of Victoria, PO Box 3055, Station CSC, Victoria, BC V8W 3P6, Canada*
[12]*Macquarie University, Sydney, NSW 2109, Australia*
[13]*Mullard Space Science Laboratory, University College London, Holmbury St Mary, Dorking RH5 6NT, UK*
[14]*Department of Physics and Astronomy 'Galileo Galilei', Padova University, Vicolo dell Osservatorio 2, I-35122 Padova, Italy*
[15]*Anglo-Australian Observatory, PO Box 296, Epping, NSW 1710, Australia*
[16]*Johns Hopkins University, 3400 N Charles Street, Baltimore, MD 21218, USA*
[17]*Faculty of Mathematics and Physics, University of Ljubljana, Jadranska 19, 1000 Ljubljana, Slovenia*

ABSTRACT

The RAdial Velocity Experiment survey, combined with proper motions and distance estimates, can be used to study in detail stellar kinematics in the extended solar neighbourhood (solar suburb). Using 72 365 red-clump stars, we examine the mean velocity components in 3D between $6 < R < 10$ kpc and $-2 < Z < 2$ kpc, concentrating on north–south differences. Simple parametric fits to the (R, Z) trends for V_ϕ and the velocity dispersions are presented. We confirm the recently discovered gradient in mean Galactocentric radial velocity, V_R, finding that the gradient is marked below the plane ($\delta\langle V_R\rangle/\delta R = -8$ km s^{-1} kpc^{-1} for $Z < 0$, vanishing to zero above the plane), with a Z gradient thus also present. The vertical velocity, V_Z, also shows clear, large-amplitude ($|V_Z| = 17$ km s^{-1}) structure, with indications of a rarefaction–compression pattern, suggestive of wave-like behaviour. We perform a rigorous error analysis, tracing sources of both systematic and random errors. We confirm the north–south differences in V_R and V_Z along the line of sight, with the V_R estimated independent of the proper motions. The complex three-dimensional structure of velocity space presents challenges for future modelling of the Galactic disc, with the Galactic bar, spiral arms and excitation of wave-like structures all probably playing a role.

Key words: Galaxy: kinematics and dynamics – solar neighbourhood – Galaxy: structure.

1 INTRODUCTION

The more we learn about our Galaxy, the Milky Way, the more we find evidence that it is not in a quiescent, stable state. Rather, the

⋆ E-mail: mary@aip.de
† Senior CIfAR Fellow.

emerging picture is of a Galaxy in flux, evolving under the forces of internal and external interactions. Within the halo, there is debris left by accretion events, the most significant being the Sagittarius stream (Majewski et al. 2003) at a mean distance of $d \sim 20$–40 kpc associated with the Sagittarius dwarf galaxy (Ibata, Gilmore & Irwin 1994). In the intersection of halo and disc there are also indications of accretion debris, such as the Aquarius stream ($0.5 < d < 10$ kpc; Williams et al. 2011) as well as local halo streams such as the Helmi stream ($d < 2.5$ kpc; Helmi et al. 1999). While within the disc itself there is evidence of large-scale stellar overdensities: outwards from the Sun at a Galactocentric distance of $R = 18$–20 kpc there is the Monoceros Stream (Newberg et al. 2002; Yanny et al. 2003), inwards from the Sun ($d \sim 2$ kpc) there is the Hercules thick-disc cloud (HTDC; Larsen & Humphreys 1996; Parker, Humphreys & Larsen 2003; Parker, Humphreys & Beers 2004; Larsen, Humphreys & Cabenela 2008). The origin of all such structures is not yet fully understood: possible agents for the Monoceros ring are tidal debris (see e.g. Penarrubia et al. 2005), the excitation of the disc caused by accretion events (e.g. Kazantzidis et al. 2008) or the Galactic warp (Momany et al. 2006), while Humphreys et al. (2011) conclude that the Hercules cloud is most likely due to a dynamical interaction of the thick disc with the Galaxy's bar.

Velocity space also exhibits structural complexity. In the solar neighbourhood, various structures are observed in the distribution of stars in the *UV* plane, which differs significantly from a smooth Schwarzschild distribution (Dehnen 1998). These features are likely created by the combined effects of the Galactic bar (Raboud et al. 1998; Dehnen 1999; Famaey et al. 2007; Minchev et al. 2010) and spiral arms (De Simone, Wu & Tremaine 2004; Quillen & Minchev 2005; Antoja et al. 2009) or both (Chakrabarty 2007; Quillen et al. 2011). Dissolving open clusters (Skuljan, Cottrell & Hearnshaw 1997; De Silva et al. 2007) can also contribute to structure in the *UV* plane. Finally, velocity streams in the *UV* plane can be explained by the perturbative effect on the disc by recent merger events (Minchev et al. 2009; Gómez et al. 2012a).

Venturing beyond the solar neighbourhood into the solar suburb, Antoja et al. (2012) used data from the RAdial Velocity Experiment (RAVE) (Steinmetz et al. 2006) to show how these resonant features could be traced far from the Sun, up to 1 kpc from the Sun in the direction of antirotation and 0.7 kpc below the Galactic plane. Additionally, Siebert et al. (2011a, hereafter S11), showed based on RAVE data that the components of stellar velocities in the direction of the Galactic Centre, V_R, is systematically non-zero and has a non-zero gradient $\delta \langle V_R \rangle / \delta R < -3 \, \mathrm{km \, s^{-1} \, kpc^{-1}}$. A similar effect was seen in the analysis of 4400 RAVE red-clump (RC) giants by Casetti et al. (2011). The cause of this streaming motion has been variously ascribed to the bar, spiral arms and the warp in conjunction with a triaxial dark-matter halo, or a combination of all three. Recently, Siebert et al. (2012, hereafter S12) have used density-wave models to explore the possibility that spiral arms cause the radial streaming, and were able to reproduce the gradient with a two-dimensional model in which the Sun lies close to the 4:1 ultraharmonic resonance of two-arm spiral, in agreement with Quillen & Minchev (2005) and Pompéia et al. (2011). While structure in the *UV* plane smears out with the increase of sample depth (at $d > 250$ pc), Gómez et al. (2012a,b) showed that energy–angular momentum space preserves structure associated with 'ringing' of the disc in response to a minor merger event for distances around the Sun as large as 3 kpc, consistent with the Sloan Extension for Galacitic Understanding and Exploration (SEGUE) and RAVE coverage.

In this paper, we examine the kinematics of the red-clump giants in the three-dimensional volume surveyed by RAVE, focusing par-

ticularly on differences between the northern and southern sides of the plane. The full space velocities are calculated from RAVE line-of-sight velocities (V_{los}), literature proper motions and photometric distances from the red clump. We have sufficient stars from the RAVE internal data set for the stellar velocity field to be explored within the region $6 < R < 10$ kpc and $-2 < Z < 2$ kpc. While studies such as Pasetto et al. (2012a,b) distinguish between thick- and thin-disc stars, we do not. Distinguishing between the thin, thick disc and halo require either kinematic or chemical criteria, each of which have their individual issues and challenges, which we wish to avoid. Rather, our aim here is to describe the overall velocity structure of the solar neighbourhood in a pure observational/phenomenological sense. The interpretation of this based on thin- or thick-disc behaviour is then secondary.

In S11, V_R as a function of (X, Y) was examined. Here, we extend this analysis to investigate particularly the Z dependence of V_R, as well as the other two velocity components, V_ϕ and V_Z, with a simple parametric fit for V_ϕ presented. We find that the average values of V_R and V_Z show a strong dependence on three-dimensional position. We compare these results to predictions of a steady-state, axisymmetric Galaxy from the GALAXIA (Sharma et al. 2011) code. To visualize the 3D behaviour better, various projections are used. Further, the detection by S11 of the gradient in V_R using only line-of-sight velocities is re-examined in light of the results seen in 3D, extending the analysis to include V_Z. As an aside, parametric fits to the velocity dispersions are presented.

The paper also includes a thorough investigation into the effects of systematic and measurement errors, which almost everywhere dominate Poisson noise. The assumptions used to calculate photometric distances from the red clump are examined in some detail, where we model the clump using GALAXIA. The effects of using alternative sources of proper motion are shown in comparison with the main results, as we found this to be one of the largest systematic error sources.

The paper is organized as follows. In Section 2, we discuss our overall approach for the kinematic mapping, the coordinate systems used and initial selection from RAVE. In Section 3, we present a detailed investigation into the use of the red-clump stars as a distance indicator, where we introduce a GALAXIA model of the red clump to model the distance systematics. In Section 4, we present our error analysis, investigating systematic error sources first before discussing measurement errors, Poisson noise and the final cuts to the data using the error values. In Section 5, we examine the 3D spatial distribution of our data before going on in Section 6 to investigate the variation for V_R, V_ϕ and V_Z over this space. Also presented are the variations in velocity dispersions with (R, Z) and a simple functional fit to these trends. In Section 7, we use the line-of-sight method to investigate the V_R and V_Z trends towards and away from the Galactic Centre, while finally, Section 8 contains a summary of our results.

2 RED-CLUMP KINEMATICS WITH RAVE DATA

2.1 Coordinate systems and Galactic parameters

As we are working at large distances from the solar position, we use cylindrical coordinates for the most part, with V_R, V_ϕ and V_Z defined as positive with increasing R, ϕ and Z, with the latter towards the North Galactic Pole (NGP). We also use a right-handed Cartesian coordinate system with X increasing towards the Galactic Centre, Y in the direction of rotation and Z again positive towards the NGP.

The Galactic Centre is located at $(X, Y, Z) = (R_\odot, 0, 0)$. Space velocities, UVW, are defined in this system, with U positive towards the Galactic Centre.

To aid comparison with the predictions of GALAXIA (see Section 2.3), we use mostly the parameter values that were used to make the model for which GALAXIA makes predictions. Thus, the motion of the Sun with respect to the Local Standard of Rest (LSR) is taken from Schönrich, Binney & Dehnen (2010), namely $U_\odot = 11.1$, $V_\odot = 12.24$, $W_\odot = 7.25$ km s^{-1}. The LSR is assumed to be on a circular orbit with circular velocity $V_{\text{circ}} = 226.84$ km s^{-1}. Finally, we take $R_\odot = 8$ kpc. The only deviation from GALAXIA's values is that they assumed that the Sun is located at $Z = +15$ pc, while we assume $Z = 0$ pc.

S11 explored the variation of the observed V_R gradient on the values of V_{circ} and $R_\odot$, finding that changing these parameters between variously accepted values could reduce but not eliminate the observed gradient in V_R. We do not explore this in detail in this paper but note that the trends that we observe are similarly affected by the Galactic parameters; amplitudes are changed but the qualitative trends remain the same.

2.2 RAVE data

The wide-field RAVE survey measures primarily line-of-sight velocities and additionally stellar parameters, metallicities and abundance ratios of stars in the solar neighbourhood (Steinmetz et al. 2006; Zwitter et al. 2008; S11; Boeche et al. 2011). RAVE's input catalogue is magnitude limited $(8 < I < 13)$ and thus creates a sample with no kinematic biases. To the end of 2012 RAVE had collected more than 550 000 spectra with a median error of 1.2 km s^{-1} (Siebert et al. 2011b).

We use the internal release of RAVE from 2011 October which contains 434 807 Radial Velocities (RVs) and utilizes the revised stellar parameter determination (see the DR3 paper, Siebert et al. 2011b, for details). We applied a series of cuts to the data. First, those stars flagged by the Matijevič et al. (2012) automated spectra classification code as having peculiar spectra were excluded. This removes most spectroscopic binaries, chromospherically active and carbon stars, spectra with continuum abnormalities and other unusual spectra. Further cuts restricted our sample to stars with signal-to-noise ratio STN > 20 (STN is calculated from the observed spectrum alone with residuals from smoothing, see section 2.2 of the DR3); Tonry & Davis (1979) cross-correlation coefficient $R > 5$, $|\mu_\alpha, \mu_\delta| < 400$ mas yr^{-1}, $e\mu_\alpha, e\mu_\delta < 20$ mas yr^{-1}, RV < 600 km s^{-1} (see Section 4.4) and stars whose SpectraQualityFLAG is null. Where there are repeat observations, we randomly select one observation for each star. With this cleaning, the data set has 293 273 unique stars with stellar parameters from which to select the red clump.

In some fields, at $|b| < 25°$ the RAVE selection function includes a colour cut $J - K > 0.5$ with the object of favouring giants. We imposed this colour cut throughout this region to facilitate the comparison to predictions by GALAXIA. The selection of red-clump stars is unaffected by this cut. Additional data cuts and selections were performed later in the analysis and are broadly (a) the selection of red-clump giants (Section 3.3), and (b) removal of stars with large extinction/reddening (Section 4.1.5) and data bins with large errors in measurements of mean velocity (Section 4.4).

As a sample with alternative distance determinations, we also used an internal release with stellar parameters produced by the pipeline that was used for the third Data Release (VDR3) and the method of Zwitter et al. (2010) from 2011 September with 334 409

objects. We cleaned the sample as above, leaving us with 301 298 stars.

A newer analysis of RAVE data is presented in the 4th RAVE data release (Kordopatis et al. 2013). This applies an updated version of the Kordopatis et al. (2011) pipeline to RAVE spectra. Selecting red-clump stars using the stellar parameters from this pipeline does not produce significantly different results to those selected using the VDR3 pipeline above; the conclusions of this paper are unaffected by the pipeline used for the red-clump selection.

2.3 The GALAXIA model

In Williams et al. (2011), we introduced the use of the Galaxy modelling code GALAXIA (Sharma et al. 2011) to investigate the statistical significance of the new Aquarius stream found with RAVE. In this study, we use GALAXIA both to provide predictions with which to compare our results, and to investigate the effects of contamination of the red-clump sample by stars that are making their first ascent of the giant branch (see Section 4.1.1). GALAXIA enables us to disentangle real effects from artefacts of our methodology, and further to understand the population we are examining.

Based on the Besançon Galaxy model, the GALAXIA code creates a synthetic catalogue of stars for a given model of the Milky Way. It offers several improvements over the Besançon model which increase its utility in modelling a large-scale survey like RAVE, the most significant of which is the ability to create a continuous distribution across the sky instead of discrete sample points. The elements of the Galactic model are a star formation rate (SFR), age–velocity relation, initial mass function and density profiles of the Galactic components (thin and thick disc, smooth spheroid, bulge and dark halo). The parameters and functional forms of these components are summarized in table 1 of Sharma et al. (2011).

We follow a similar methodology to that described in Williams et al. (2011) to generate a GALAXIA model of the RAVE sample, from which we select a red-clump sample following the selection criteria applied to the real data. A full catalogue was generated over the area specified by $0 < l < 360$, $\delta < 2°$ and $9 < I < 13$, with no undersampling. As described in Section 3.2, the RAVE data were then divided into three STN regimes and a sample drawn from the GALAXIA model so that, for each regime, the I-band distribution was matched to that of the RAVE sample in $5° \times 5°$ squares. The GALAXIA I band was generated after correcting for extinction.

3 THE RED CLUMP

The helium-burning intermediate-age red clump has long been seen as a promising standard candle (Cannon 1970), with its ease of identification on the HR diagram. In recent years, there has been a renewed interest in the red clump for distance determination, e.g. Pietrzyński, Gieren & Udalski (2003) studied the clump in the Local Group, down to the metal-poor Fornax dwarf galaxy. Here, we investigate the use, selection and modelling of this population in solar-suburb RAVE data.

3.1 The Red-clump K-band magnitude

The K-band magnitude of the red clump, while being relatively unaffected by extinction, has also been shown observationally to be only weakly dependent on metallicity and age (Alves 2000; Pietrzyński et al. 2003), so a single magnitude is usually assigned for all stars in the red clump. Studies such as Grocholski & Sarajedini (2002) and van Helshoecht & Groenewegen (2007) have shown

Table 1. The normalizations used for the red-clump M_{K_s} magnitudes.

Version	M_{K_s}	Source
A	−1.65	Observation: Alves (2000), Grocholski & Sarajedini (2002)
B	−1.54	Observation: Groenewegen (2008)
C	−1.64 + 0.0625|Z(kpc)|	Theory: Salaris & Girardi (2002) compared to the RAVE population

that there is some dependence on metallicity and age which can be accounted for by the theoretical model of Salaris & Girardi (2002).

If models correctly predict the systematic dependence of M_K of the red clump on metallicity and age, this would have implications for our study of kinematics in the solar suburb, for with increasing distance above the plane the metallicity will decrease and the population become older. From Burnett et al. (2011), we estimate that the population means change from $[M/\text{H}] \sim 0$, Age $= 4\,\text{Gyr}$ at $Z = 0\,\text{kpc}$ to $[M/\text{H}] \sim -0.6$, Age $= 10\,\text{Gyr}$ at $Z = |4|\,\text{kpc}$. According to Salaris & Girardi (2002), these age and metallicity changes will change the K-band absolute magnitude from $M_{K_s}(\text{RC}) = -1.64^1$ at $Z = 0\,\text{kpc}$ to $M_{K_s}(\text{RC}) = -1.39$ at $|Z| = 4\,\text{kpc}$. Hence, the distances to stars at higher Z will be systematically underestimated by ~ 10 per cent.

Furthermore, there is uncertainty regarding the average value of M_K. Alves (2000) gives $M_K(\text{RC}) = -1.61 \pm 0.03$ for local red-clump giants with *Hipparcos* distances and metallicities between $-0.5 \leq [\text{Fe/H}] \leq 0.0$. In the 2MASS system, the corresponding absolute magnitude is $M_{K_s}(\text{RC}) = -1.65 \pm 0.03$. Grocholski & Sarajedini (2002) derives a similar value of $M_K(\text{RC}) = -1.61 \pm 0.04$ for $-0.5 \leq [\text{Fe/H}] \leq 0.0$, $1.6\,\text{Gyr} \leq$ Age $\leq 8\,\text{Gyr}$ from 2MASS data of open clusters. Extending the sample of clusters, van Helshoecht & Groenewegen (2007) derived $M_K(\text{RC}) = -1.57 \pm 0.05$ for $-0.5 \leq [\text{Fe/H}] \leq 0.4$, $0.3\,\text{Gyr} \leq$ Age $\leq 8\,\text{Gyr}$. Then, using the new van Leeuwen (2007) *Hipparcos* parallaxes, Groenewegen (2008) found that the *Hipparcos* red-clump giants now give $M_{K_s}(\text{RC}) = -1.54 \pm 0.05$ ($M_K(\text{RC}) = -1.50 \pm 0.05$) over $-0.9 \leq [\text{Fe/H}] \leq 0.3$, with a selection bias, whereby accurate K magnitudes are only available for relatively few bright stars, meaning that the actual value is likely brighter. The newer values hold better agreement with the theoretical results of Salaris & Girardi (2002), who derived an average value for the solar neighbourhood of $M_{K_s}(\text{RC}) = -1.58$, derived via modelling with an SFR and age–metallicity relation.

Given the disagreement over the K-band magnitude for the clump and possible metallicity/age variations, we investigated the use of the three normalizations for M_{K_s} for our derivation of the RAVE red-clump distances. Table 1 summarizes these values, where the Version A is the standard value from Alves (2000) and Grocholski & Sarajedini (2002), while Version B is the new value from Groenewegen (2008). Version C is derived from the theoretical models of Salaris & Girardi (2002) and attempts to take into account some of the possible systematics for lower metallicity stars, where we use the variation of age and metallicity of RAVE stars described above (i.e., $M_{K_s}(\text{RC}) = -1.64$ at $|Z| = 0\,\text{kpc}$ to $M_{K_s}(\text{RC}) = -1.39$ at $|Z| = 4\,\text{kpc}$) to develop a simple linear relation of M_{K_s} with Z, where the value for each star is derived iteratively. In Section 4.1.2, we examine the effect of the different normalizations on our results.

---

[1] Here, K is used to denote K-band magnitudes in the Bessell & Brett (1989) system, while K_s is used to denote 2MASS values. The relations from Carpenter (2003) were used to convert between the two photometric systems. Note though that $J - K_S$ is shortened to $J - K$ in Section 3.2 and beyond.

Table 2. Standard deviations of the error distributions added to the GALAXIA model to match the RAVE distributions in the three STN regimes. The same seed was used for the $\log g$ and T_{eff} to mimic the error covariance.

STN regime	$\sigma(\log g)$	$\sigma(T_{\text{eff}})$	$\sigma(J - K)$
$60 \leq$ STN	0.25	25	0.01
$40 \leq$ STN < 60	0.35	110	0.01
$20 \leq$ STN < 40	0.45	150	0.01

3.2 The GALAXIA red clump

To establish the best selection method for the red-clump stars, we first tried to match the observed distribution of the selected RC stars with the prediction of GALAXIA. The errors in RAVE stellar parameters decrease with STN, so the red clump is more localized at higher STN values. Further, the errors in T_{eff} and $\log g$ are correlated. To account for this in the modelling of the clump, we split the data into three regimes: STN values between $20 < \text{STN} < 40$, $40 < \text{STN} < 60$ and $60 < \text{STN}$. We then generated GALAXIA models for each STN regime for $5° \times 5°$ squares, matching the I-band distribution of GALAXIA to that of RAVE in bins of 0.2 mag. The three models for each STN slice of the data were added together to give an overall GALAXIA model, with an STN value of 20, 40 or 60 assigned to the GALAXIA 'stars' to indicate which STN regime they were generated from. Note that, as stated in the DR2 and DR3 releases, the DENIS I-band photometry has large errors for a significant fraction of the stars. We therefore used equation (24) from the DR2 paper to calculate I magnitudes for those RAVE stars which do not satisfy the condition $-0.2 < (I_{\text{DENIS}} - J_{\text{2MASS}}) - (J_{\text{2MASS}} - K_{\text{2MASS}}) < 0.6$, as well as those that have 2MASS photometry but no DENIS values. For the models, the reddening at infinity is matched to that of the value in Schlegel map and to convert $E(B - V)$ to extinction in different photometric bands we used the conversion factors in table 6 of Schlegel, Finkbeiner & Davis (1998).

Errors were then added to the values of T_{eff}, $\log g$ and $J - K$ from GALAXIA to match the distributions in the RAVE data. The same seed was used for the random number generator for the temperature and gravity values to account for the error covariance. Table 2 gives the standard deviations of the errors that were added to the values from GALAXIA. The average $J - K$ error, 0.01, is smaller than the expected average observational error in $J - K$, $\sqrt{eJ^2 + eK_S^2} = 0.03$. An error of 0.01 in $J - K$ corresponds to an error in T_{eff} of $\sim 40\,\text{K}$ (Alonso, Arribas & Martinez-Roger 1996). Given this small value and that, unlike T_{eff}, the spread in $J - K$ does not change with STN, we opted to select the RAVE red clump in $(J - K, \log g)$.

3.3 Selection of RC stars

Fig. 1 plots the $(J - K, \log g)$ plane for the RAVE giants within $8 < I < 13$ in the three STN regimes along with the corresponding GALAXIA predictions including errors. Here, we see the clump at $J - K \sim 0.65$ and $\log g \sim 2.2$. There are some notable differences
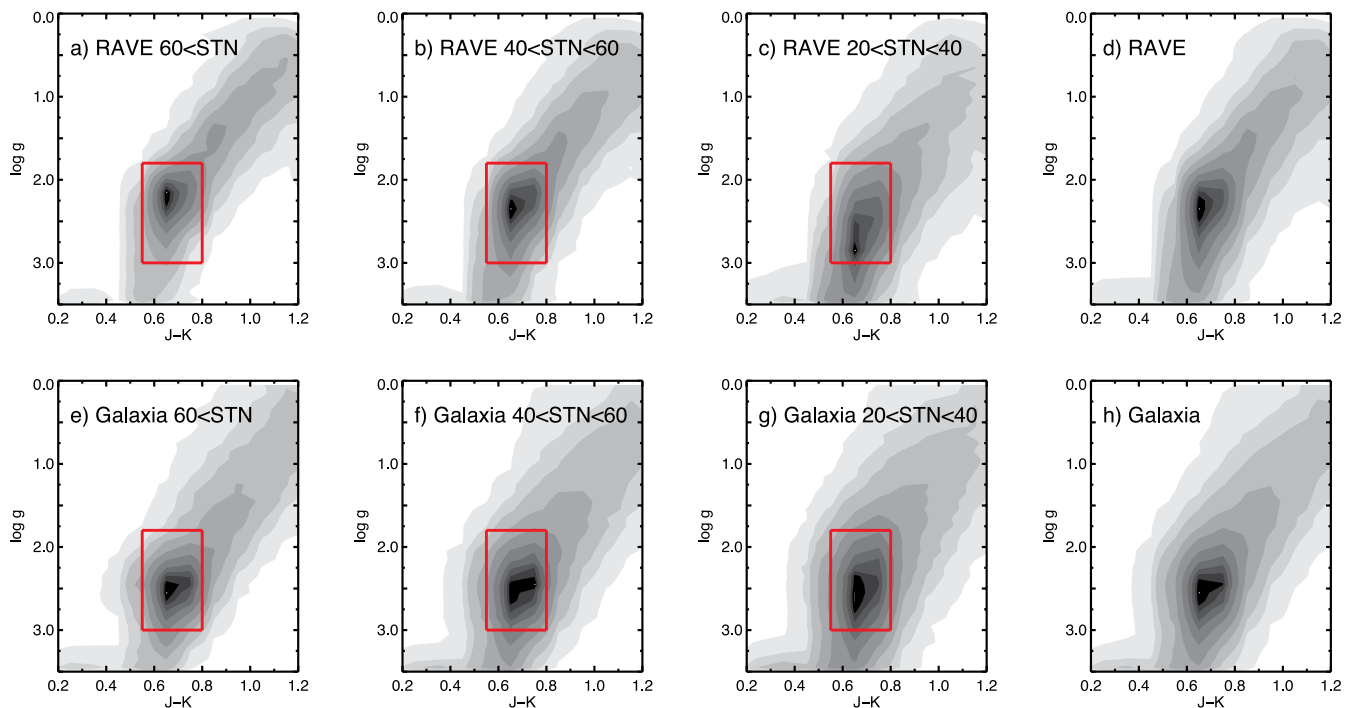
Figure 1. The $J-K$–$\log g$ plane for RAVE giants for three STN regimes (a–c) and the corresponding GALAXIA models (e and f). Panels (d) and (h) show the aggregate RAVE and GALAXIA samples, respectively. The red clump is visible as an overdensity centred at $(J-K, \log g) = (0.65, 2.2)$ and the selection for the red-clump region is outlined by the red box. There is a larger movement of the red-clump position in $\log g$ with decreasing STN for RAVE stars compared to GALAXIA.

between the models and the observed distributions. First, the position of the clump in $\log g$ decreases with decreasing STN for the RAVE stars. This change is not matched by GALAXIA: the predicted distribution has mean $\log g \sim 2.4$. With increasing dispersion at lower STN it elongates but does not shift. Thus, the effect seen in the RAVE data appears not to be astrophysical in origin but rather a result of the parameter determination from RAVE spectra (for a discussion on systematic trends of stellar parameter estimates with SNR, see DR3). Also, there is an absence of horizontal-branch stars below $J-K < 0.55$ in the RAVE data relative to the prediction by GALAXIA. This latter difference does not affect our results as they are not included in the selection region.

We select the red clump as those stars within $0.55 \leq J-K \leq 0.8$, $1.8 \leq \log g \leq 3.0$. We do not include a STN dependence as extending the selection box further up in gravity will mean an increased fraction of subgiants in the sample and thus erroneous distances. The red box in Fig. 1 displays the selection criteria, where we see that for $20 < \text{STN} < 40$ some of the clump is cut off at higher values of $\log g$. Applied to our entire cleaned RAVE set, this selection yields 78 019 stars. A sample of red-clump stars were also selected from the GALAXIA model in the same way, with a slightly smaller number of 73 594 'stars'.

Fig. 2 gives the distributions of the entire RAVE data set and red-clump stars in I, V_{los} and overall proper motion, $\mu = \sqrt{\mu_\alpha^2 + \mu_\delta^2}$. The distributions from GALAXIA are also given, with an additional spread of $2\,\text{km s}^{-1}$ and $2.7\,\text{mas yr}^{-1}$ added to the GALAXIA line-of-sight velocity and proper motion, respectively, to simulate the observational uncertainties. These values give the average value of the error in these quantities for the RAVE catalogue stars. Here, we see that GALAXIA reproduces quite well the basic distributions of the two observational kinematic parameters which affirms our use of it in comparisons. The small difference in the proper-motion

distribution could suggest that the actual errors in proper motion are slightly larger than estimated.

4 ERROR ANALYSIS

The most problematic errors are systematic ones. There are multiple ways that these can be introduced into the kinematics. We examine these in some detail before discussing measurement errors in Section 4.2, Poisson noise in Section 4.3 and the final data cuts in Section 4.4.

4.1 Systematic error sources

4.1.1 Contamination by first-ascent giants

In the $(J-K, \log g)$ plane, the red clump is overlaid on the first-ascent giant branch (see Fig. 1). Our selection criteria therefore also select first-ascent giants, including some subgiants, which can lead to distance and velocity errors. To assess how this contamination affects our distances and kinematics, we use the red-clump selected stars from the GALAXIA model and compute a distance to them assuming a single red-clump magnitude. These results can then be compared to the true values for the model stars. GALAXIA uses mainly Padova isochrones and with a median red-clump K-band magnitude of $M_{K_s}(\text{RC}) = -1.50$. This is slightly different to that applied above to our data, but is not significant as we are only performing an internal comparison with GALAXIA.

Fig. 3(a) shows the histogram of the parallax errors. The distributions can be decomposed into two Gaussians, one representing the red clump and the other first-ascent giants. Note that the histogram of distance errors does not have such a tidy Gaussian decomposition, hence why we work with the parallax errors. The spread in
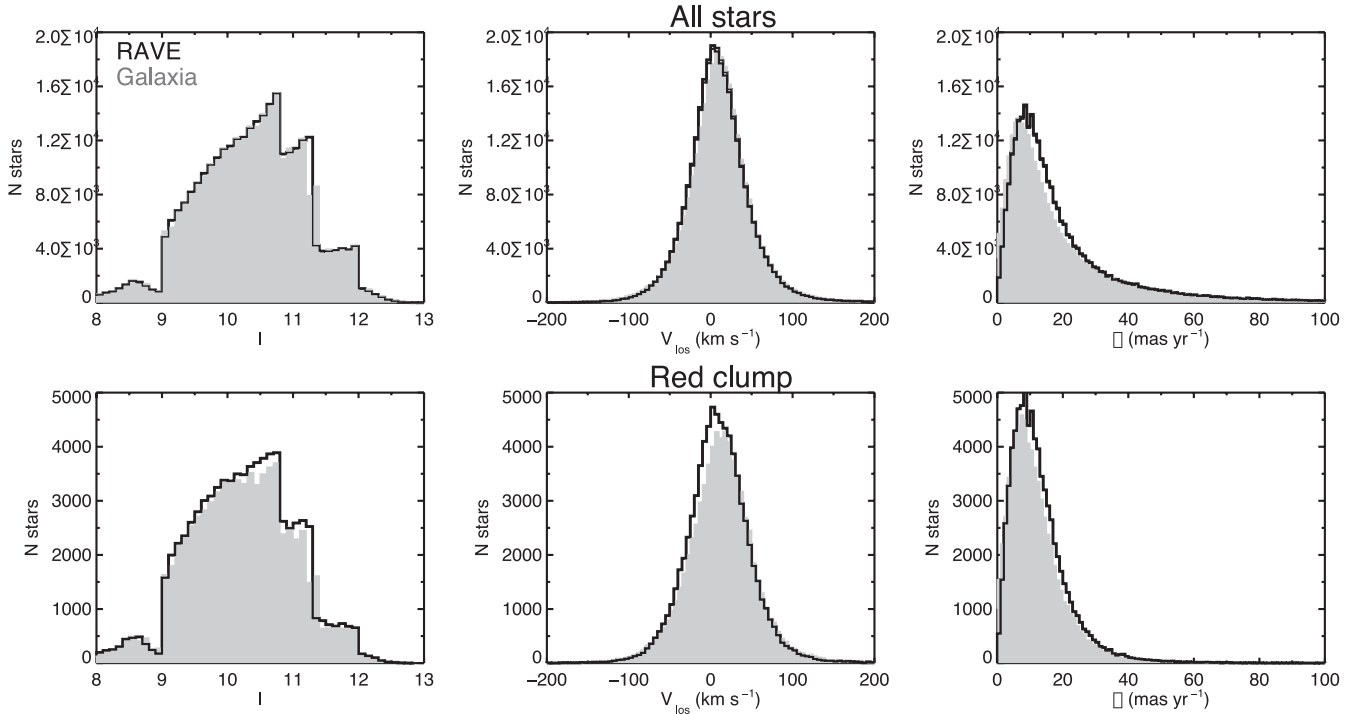
Figure 2. The distributions for I, $V_{\rm los}$ and overall proper motion μ for the entire sample of unique, cleaned RAVE stars between $8 < I < 13$ (top) and those selected as part of red-clump selected stars (bottom). The I magnitudes for the RAVE stars are from DENIS, apart from those with problematic values as discussed in Section 3.2. The GALAXIA model reproduces the two observational kinematic distributions.
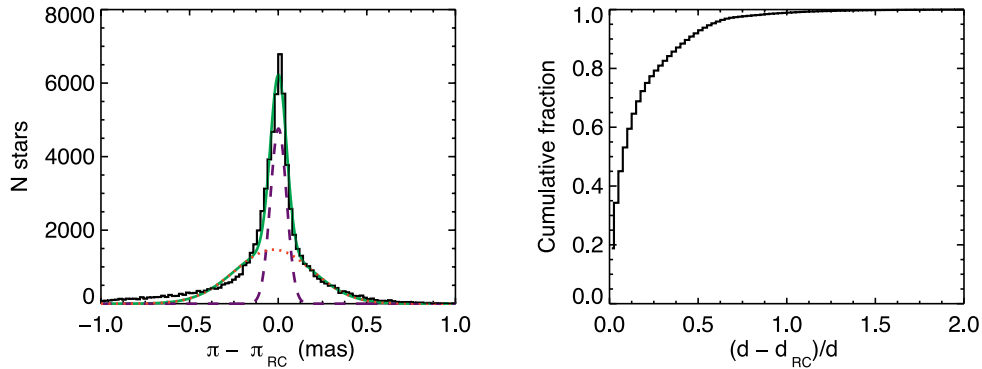

Figure 3. (a) Histogram of parallax error for GALAXIA model stars caused by assuming a single red-clump magnitude for stars selected in the red-clump region. The distribution is decomposed into two Gaussians: one associated with the true RC (dashed blue line) and one with the first ascent giants (dotted red line). Their sum is given by the solid green line. (b) The cumulative distribution of the corresponding distance errors.

the red-clump values is caused by the clump's distribution in age and metallicity; the average M_K value chosen is not true for all red-clump stars. The first-ascent giants have larger errors because while their $\log g$ values may overlap with the clump, their absolute K-band magnitude can be quite different. From this decomposition, we estimate that the $\sim$40 per cent of selected stars are actually red-clump stars and the rest are first-ascent giants. Fortunately however, the mean of the background distribution is very similar to that of the red clump, with a systematic shift of only $\sim$2 per cent in distance. In Fig. 3(b), we plot the cumulative distribution of the distance errors. From this, we can see that despite the high level of contamination, 80 per cent of stars have distances errors of less that 25 per cent.

To establish just how these distance errors affect our results, we calculated ($V_{\rm R}$, V_ϕ, V_Z) for stars in the solar cylinder ($7.5 <$

$R\,{\rm kpc}^{-1} < 8.5$) from the pseudo-data produced by GALAXIA using both the true distance to each star, and the distance one infers from the star's apparent magnitude and a single RC M_K. The upper panels of Fig. 4 show the resulting plots of mean velocity components as a function of $|Z|$. In the panels for $V_{\rm R}$ and V_Z, the differences between the velocities from true distances (solid line) and from ones derived from a single absolute magnitude (dashed line) are noticeable only at the limits of the surveyed region. In the case of V_ϕ, the single value of M_K leads to a consistent underestimation by $\sim$5 km s^{-1}. The lower panels of Fig. 4 show the corresponding results for stars that lie within 0.5 kpc of the plane, binned in R. Again the impact on $V_{\rm R}$ and V_Z of using a single absolute magnitude is evident only at the survey limits. We conclude that the use of a single value of M_K does not significantly compromise our results.
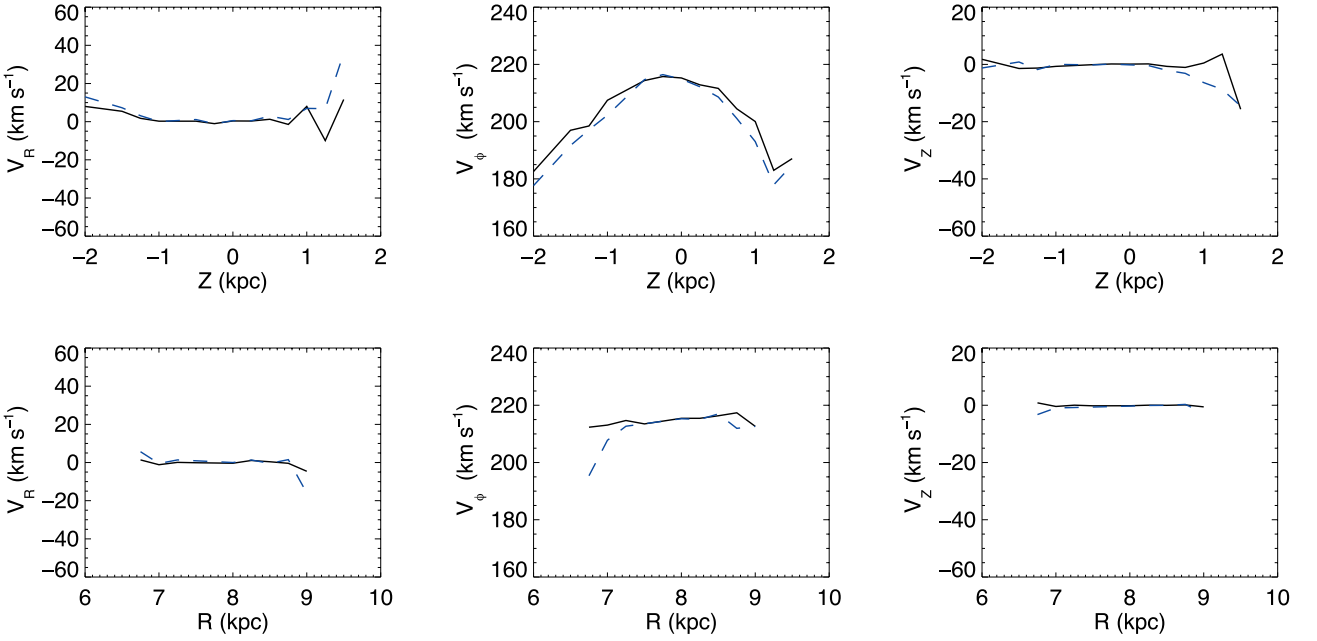
Figure 4. Comparison between simulated GALAXIA model results using the true GALAXIA model distances (solid black line) and those assuming a RC M_K magnitude (dashed blue line). The average V_R, V_ϕ and V_Z for stars within $7.5 < R < 8.5$ kpc are plotted as a function of Z (top), as well as the values for $|Z| < 0.5$ kpc as a function of R (bottom).

4.1.2 M_K normalization

In Section 3.1, we introduced three different normalizations for the M_K value for the red clump. Fig. 5 shows the effect of using these different normalizations on the average values of V_R, V_ϕ, V_Z for stars in the solar cylinder (top row of panels) and for stars within 0.5 kpc of the plane (lower row). We see that the differences in distance produced by the three normalizations has an insignificant impact on the average velocities: only at the limits of the survey, where

sample sizes are small, do the differences reach 15 km s^{-1}. Thus, the dispersion in the velocity errors, on the order of 10 km s^{-1}, caused by the single M_K assumption are averaged over and thus all but vanish. It is only those bins – the farthest ones – with the lower number of stars that show any effect.

Given that the effect of the absolute-magnitude normalization is minor, we use only normalization A for the remainder of this analysis.
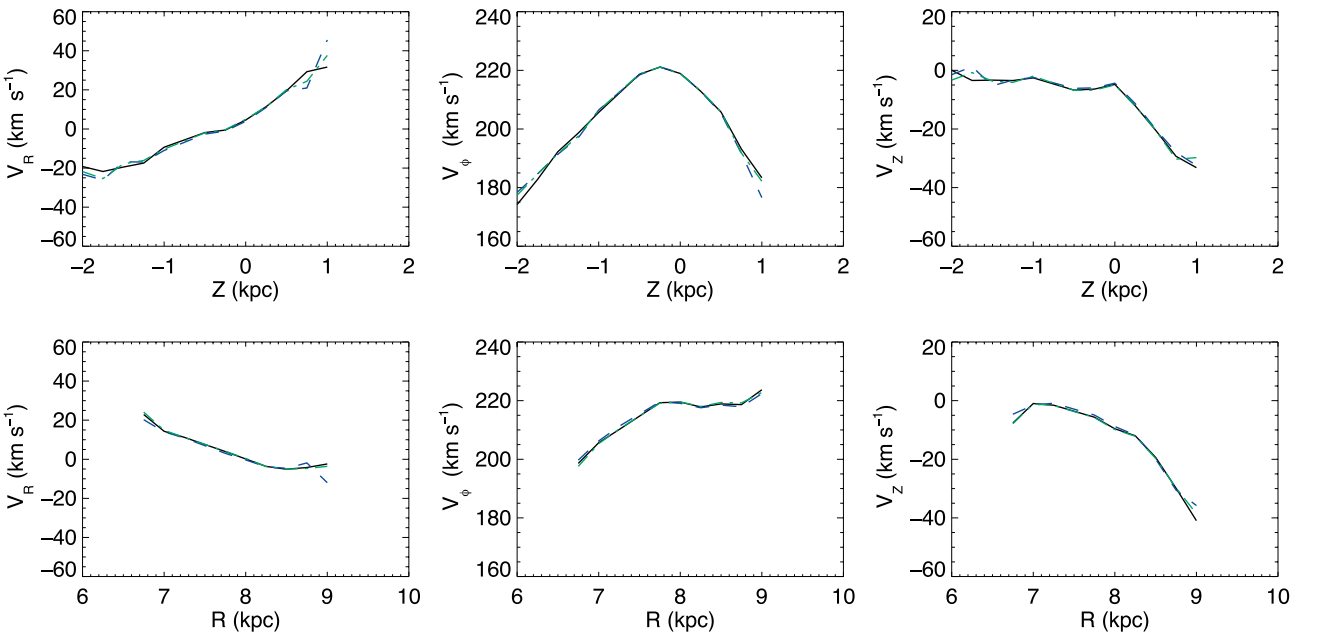

Figure 5. Comparison between the three version of the red-clump M_K normalization. The average V_R, V_ϕ and V_Z for RAVE stars within $7.5 < R < 8.5$ kpc are plotted as a function of Z (top), as well as the values for $|Z| < 0.5$ kpc as a function of R (bottom). Normalization A from Table 1 is given by the solid black line, normalization B by the blue dashed line and normalization C by the green dot–dashed line. The results are relatively insensitive to the assumption of a single M_K magnitude.
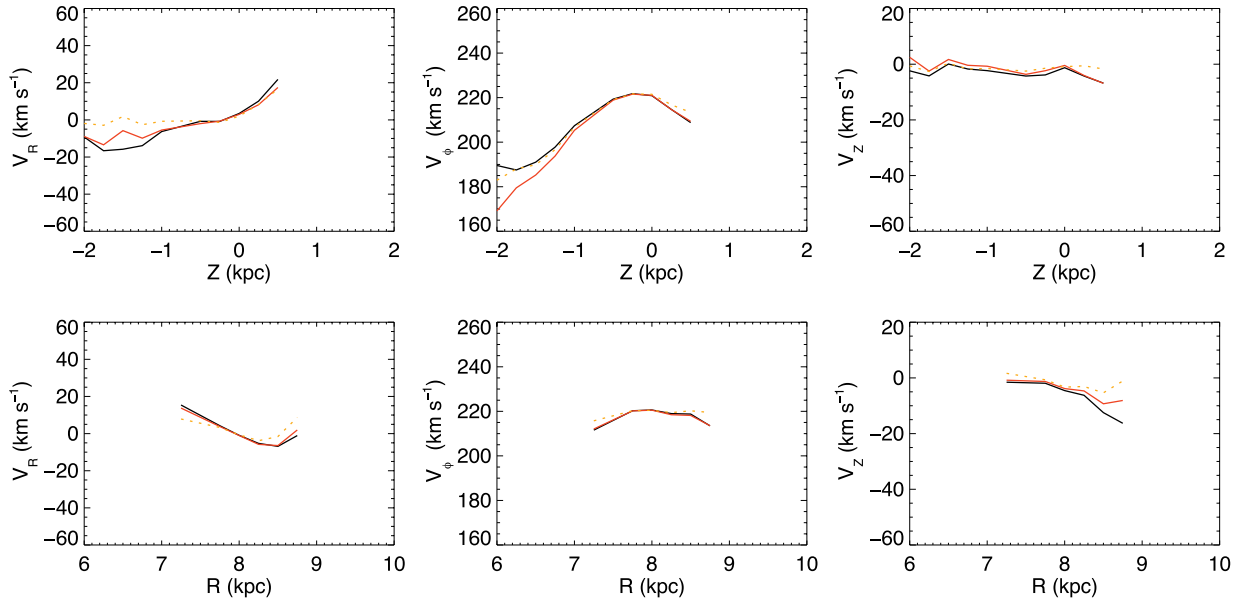
Figure 6. As in Fig. 5, but a comparison between the results using different proper-motion sources for RAVE stars with $\delta < -20°$, $-1 < Y < 0$ kpc, with RAVE catalogue proper motions (black solid line), UCAC3 proper motions (dotted orange line) and SPM4 proper motions (dash–dottted red line).

4.1.3 Proper motions

RAVE proper motions are derived from several sources, although the majority of the catalogue gives PPMX (Roeser et al. 2008) or UCAC2 (Zacharias et al. 2004) proper motions. To investigate the contribution of systematic proper-motion errors, we cross-matched with two additional proper-motion catalogues, the third US Naval Observatory CCD Astrograph Catalog, UCAC3 (Zacharias et al. 2010), and the Yale/San Juan Southern Proper Motion Catalog, SPM4 (Girard et al. 2011). The UCAC3 proper motions suffer from strong plate-dependent systematic distortions north of $\delta = -20°$ (Roeser, Demleitner & Schilbach 2010), and so we exclude stars with $\delta > -20°$ in this catalogue.

Fig. 6 shows the mean values of V_R, V_ϕ and V_Z with R and Z for stars below $\delta = -20°$, $-1 < Y < 0$ kpc calculated using the three sources of proper motions, where the restrictions in δ and Y were made to keep as uniform as possible the fractions of stars that have entries in each of the three catalogues. The mean velocities do change with proper-motion source, with the discrepancies largest between RAVE proper motions and those from the SPM4 catalogue. The divergence is largest for $Z < -1$ kpc for V_R and V_ϕ with differences up to 20 km s^{-1} in V_ϕ. Some of these variations may be the result of different coverage of the sample volume – which we have tried to minimize with the restrictions on δ, Y above. Nevertheless, it does indicate that the proper motions are a significant source of systematic error.

It is difficult to say a priori which catalogue is closer to the truth; a detailed comparison is beyond the scope of this paper. Given that the systematic differences between proper-motion catalogues can cause significant differences in the derived velocities, we use all three proper-motion catalogues in our further analysis, concentrating on the two most divergent proper motions, namely those in the RAVE and SPM4 catalogues.

4.1.4 Binary stars

Two types of spectroscopic binaries can potentially affect our results; single-lined spectroscopic binary (SB1) stars and double-lined spectroscopic binaries (SB2) stars. Both kinds introduced an addi-

tional velocity variation to the sample, with the magnitude much larger for SB2 stars. For the SB2 stars, there is the additional problem that the RAVE processing pipeline assumes that each observed spectrum is that of a single star.

Matijevič et al. (2011) use repeat observations to estimate the fraction of SB1 stars in the RAVE sample, finding a lower limit of 10–15 per cent of the sample consists of SB1 stars. The technique is biased towards shorter period binaries, but can be used to gauge the contribution to the measured dispersions from SB1 stars. In Matijevič et al. (2011), the mode of the distribution in the velocity variation from the SB1 stars is 6 km s^{-1}. Undetected, long-period binary stars will have smaller velocity variations. Thus, the small additional velocity dispersion on a limited fraction of the red-clump stars from SB1 sources can be neglected, especially as we are measuring mean velocities in this paper. The fraction of SB2 stars in RAVE is much smaller; Matijevič et al. (2010) estimate 0.5 per cent of the sample are SB2 stars. Many of these are flagged however, as well as any other peculiar stars, and have been removed from the sample. Unresolved SB2 stars are fortunately rare (Matijevič et al. 2010) and these and the remaining SB2 stars do not affect our results substantially.

4.1.5 Extinction correction

As in Williams et al. (2011), extinction is calculated iteratively from the distances using Schlegel et al. (1998) dust maps and assuming a Galactic dust distribution as in Beers et al. (2000). Note that the maps were adjusted using the correction of Yasuda, Fukugita & Schneider (2007). The extinction reaches relatively large values of $A_K > 0.1$ for $|b| < 10°$. However, the effect on the velocities is minor; the effect of the extinction correction on the total space velocity is greater than 5 km s^{-1} in only 1.6 per cent of red-clump stars. These stars were excluded from further analysis, leaving 72 365 stars in our red-clump sample.

4.2 Measurement errors

The non-systematic sources of errors in the kinematics can be broadly broken into (i) the contribution of random uncertainties

Table 3. Cuts on the data adopted for this data analysis.

Cut	Reason
$\sqrt{(V_R^2 + (V_\phi - 220)^2 + V_Z^2)} < 600\,\mathrm{km\,s^{-1}}$	Remove outlier velocities
$|V_\phi - 220| < 600\,\mathrm{km\,s^{-1}}$	Remove outlier velocities
$e_{\mu_\alpha},\ e_{\mu_\delta} < 20\,\mathrm{mas\,yr^{-1}}$	Remove outlier proper motions
$\mu_\alpha,\ \mu_\delta < 400\,\mathrm{mas\,yr^{-1}}$	Remove high proper-motion stars
$e_d/d < 1$	Zwitter only, remove large distance error stars

in the measurements and (ii) the finite sample size for each volume bin. We will examine each of these in turn, before discussing any kinematic cuts that were applied to the data.

The Monte Carlo method of error propagation enables an easy tracking of error covariances, so we employ it here by generating a distribution of 100 test particles around each input value of distance, proper motion, line-of-sight velocity[2] and then calculating the resulting points in (V_R, V_ϕ, V_Z). We assume that the proper motions and line-of-sight velocities have Gaussian errors with standard deviations given by the formal errors for each star. For the distribution in distance for each star however, we generate a double-Gaussian distribution in the parallax as in Fig. 3, which we then invert to derive the distance distribution. This takes into account the fact that errors in distance are due both to the intrinsic width of the RC and the misclassification of other giants. The ratio between the RC and first-ascent giants for GALAXIA model stars changes with distance, where we found a smaller amount of contaminants for $d > 1\,\mathrm{kpc}$. The double-Gaussian in parallax then has dispersions (0.05, 0.26) mas at a ratio of 2: 1 for $d \leq 1\,\mathrm{kpc}$ and 4: 1 for $d > 1\,\mathrm{kpc}$.

4.3 Poisson noise

In each of the bins that are used to calculate the mean velocities, there are a finite number of stars N, so Poisson noise contributes to the errors in the derived kinematic properties. These errors scale as $1/\sqrt{N}$. To establish the error contribution from this source, we used Bootstrap case resampling with replacement: for each kinematic quantity, we derived a distribution in the values by randomly resampling from the distribution of values in the bin. The variance in each value could then be calculated from the resulting distribution. Poisson errors can dominate over measurement errors in bins at large distances that contain very few stars.

To ensure that Poisson errors do not dominate our plots, we only use bins which have $N_{\mathrm{stars}} > 50$ and only include those points that have errors in the mean of less than $5\,\mathrm{km\,s^{-1}}$ (see Section 4.4).

4.4 Data cuts

There are several ways in which to prune the data to those that are deemed more reliable. However, pruning is liable to introduce kinematic biases. We investigated the effects on the measured velocities of trimming data via (a) proper motion, (b) error in proper motion, (c) distance errors, (d) magnitude of total velocity and (e) total velocity error, eV_{total}. In general, we found that as we increase the cut-off point, there is a steady increase in velocity dispersion and fluctuations in the average velocity, asymptotically approaching a value as the number of stars approaches the full sample. It

is therefore difficult to justify cuts that remove a significant proportion of stars. We therefore introduced cuts that remove only the outlier values, as given in Table 3, and we do not perform a cut on eV_{total}.

Since we seek only to follow trends with R, Z, we do not distinguish between halo, thick- and thin-disc stars. The cuts in total velocity therefore aim to be inclusive of halo stars; the $600\,\mathrm{km\,s^{-1}}$ limit is $\sim 3\sigma$ the halo dispersion of $213\,\mathrm{km\,s^{-1}}$ (Vallenari et al. 2006). An additional cut in V_ϕ is also introduced to limit ourselves to stars that have plausible rotation velocities.

In our analysis, we bin the data in physical space, calculating the means and dispersion in each bin. A further data cut was performed post-binning. For each bin, we calculate the mean $\langle V_R \rangle$, $\langle V_\phi \rangle$, $\langle V_Z \rangle$. For each of these we also calculate an error in the mean, given by standard error propagation as

$$e_{\langle V_q \rangle} = \frac{1}{N}\sqrt{\sum e_{V_q,i}^2}, \tag{1}$$

where $q = R, \phi, Z$ and $i = 1, \ldots, N$, with N the number of stars in the average. The values $e_{V_q,i}$ are given by the MC propagation described in Section 4.2. We remove bins with large errors, i.e. $e_{\langle V_q \rangle} > 5\,\mathrm{km\,s^{-1}}$. This affects only peripheral points at large distances from the Sun.

5 SPATIAL DISTRIBUTION

Before examining the velocity trends it is helpful to examine the spatial distribution, to see which regions the RAVE red-clump selection function samples. Fig. 7 gives the XYZ distribution for the RAVE red-clump stars, where we have differentiated between stars above and below the plane for clarity. Due to RAVE's magnitude limit, the red-clump stars sample a region between $0.3 < d < 2.8\,\mathrm{kpc}$. This, combined with RAVE's uneven sky coverage between the Northern and Southern Galactic hemispheres, means that the sample region is mostly outside $d > 0.5\,\mathrm{kpc}$ and quadrants 1 and 2 above the plane are not sampled.

As in S11 and S12, we also plot the location of the spiral arms as inferred from the CO maps of Englmaier et al. (2008). Going from outer to inner (left to right), the arms are the Perseus, Sagittarius–Carina and Scutum–Centaurus arms. We see that our sample misses the Scutum–Centaurus arms entirely, and samples above and below the other two spiral arms.

Another significant nearby feature is the HTDC (Larsen & Humphreys 1996 and Parker et al. 2003). Parker et al. (2003) detected it via star counts in the region $l = \pm(20°–55)°$ both above and below the plane at latitudes $b = \pm(25°–45)°$. This is in quadrant 1. Recently, Larsen, Cabenela & Humphreys (2011) reported that the HTDC starts at $(X, Y) = (0.5, 0.5)\,\mathrm{kpc}$ in our coordinates, for $0.5 < |Z| < 1.0\,\mathrm{kpc}$. From Fig. 7, we can see that the RAVE sample in the south intersects with this location of the HTDC. Jurić et al. (2008) also found the HTDC in the location $(X', Y', Z') = (6.25, -2-0, 1-2)\,\mathrm{kpc}$, corresponding

---

[2] The positions of the stars are assumed to have negligible errors.
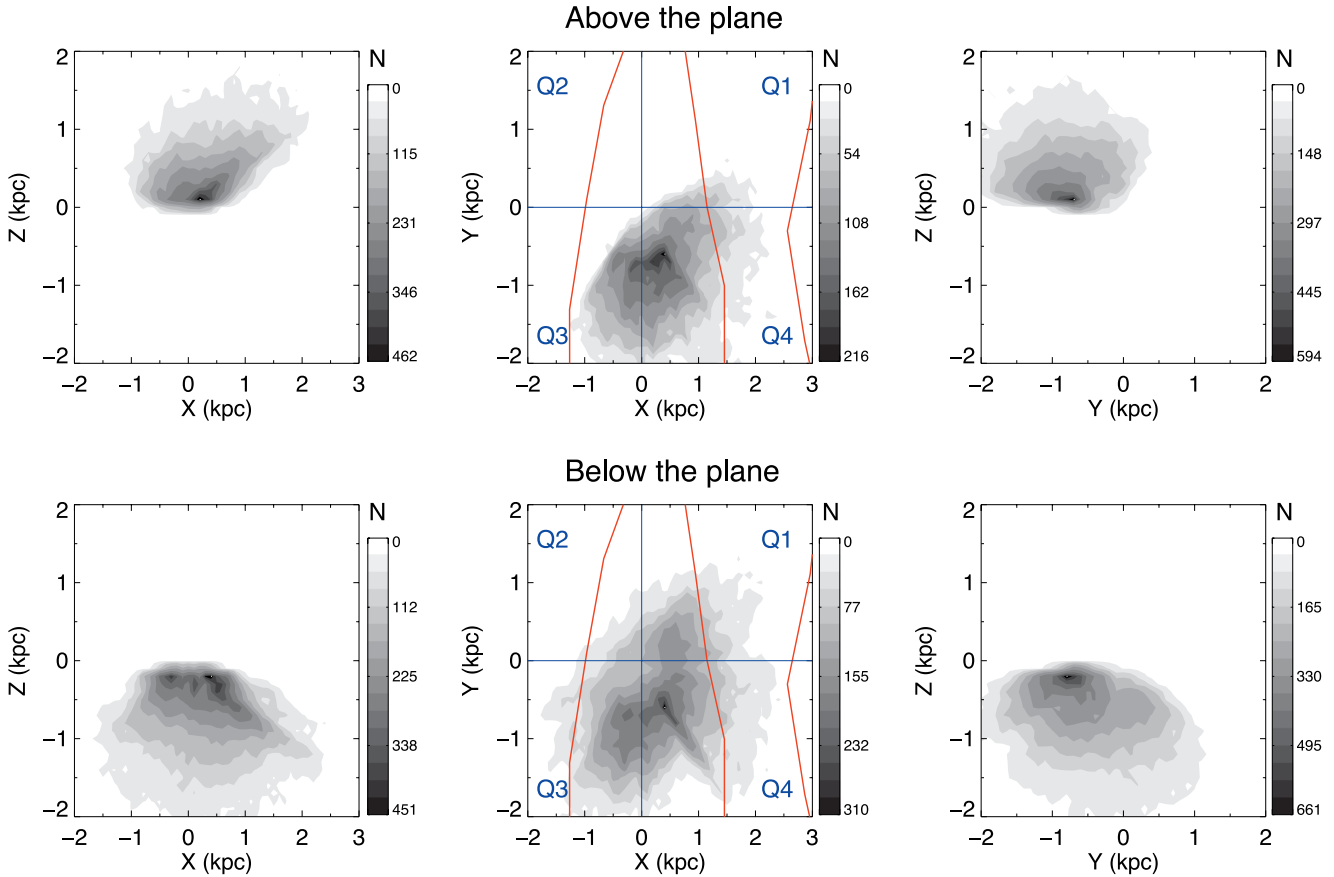
Above the plane

Below the plane

Figure 7. The XYZ distribution of RAVE red-clump giants, split into samples above the plane (top) and below the plane (bottom). The position of the spiral arms inferred from the CO maps of Englmaier, Pohl & Bissantz (2008) are plotted (red lines), giving from left to right the Perseus, Sagittarius–Carina and Scutum–Centaurus arms. The four Galactic quadrants are also delimited and labelled (Q1–Q4) in the central XY plot. Note that the diagonal overdensity of stars in quadrant 4 is purely caused by a greater number of observations in that region.

to $(X, Y, Z) = (1.75, 0-2, 1-2)$ kpc in our coordiantes. This region is not covered by the RAVE survey so we cannot see the northern component of the HTDC. In the same paper, another stellar overdensity was found at $(X', Y', Z') = (9.5, 0.5, 1-2)$ kpc $((X, Y, Z) = (-1.5, -0.5, 1-2)$ kpc), which is just missed by the RAVE volume.

6 VELOCITY TRENDS

Fig. 8 displays the trends in mean V_R, V_ϕ, V_Z (hereafter we drop the bracket notation for averages) as functions of R for 0.5 kpc thick slices in Z using 0.5 kpc bins in R. Results are shown for three choices of proper motions: those in the RAVE, UCAC3 and SPM4 catalogues. Also shown are the results of the pseudo-data from GALAXIA: the blue line is obtained using the true distances to pseudo-stars, while the green line uses distances inferred from RC magnitudes. Fig. 9 shows the trends in V_R but with $U_\odot = 14$ km s^{-1}, to investigate the effect of changing the assumed motion of the sun with respect to the LSR on the observed gradient. Figs 10, 12 and 13 display essentially the same results as contour plots in the (R, Z) plane. However, to save space we show results only for the proper motions in the RAVE and SPM4 catalogues and for the GALAXIA pseudo-data. The plotted data are box-car averages over 200 pc × 200 pc wide boxes in (R, Z) with 100 pc increments in the coordinates of the box's centre. Finally, Fig. 14 shows the results

obtained with the proper motions in the RAVE catalogue in full 3D – V_R, V_ϕ, V_Z are averaged over boxes of size 500 × 500 × 500 pc. The centres are moved by 250 pc in X and Y and spaced by 500 pc in Z.

We now discuss the trends in each velocity component.

6.1 V_ϕ

The top two panels of Fig. 10 show that, as we might expect, V_ϕ is largest in the plane and decreases fairly symmetrically both above and below the plane. At given values of Z, V_ϕ also decreases inwards. These trends are independent of the distances used (RC or Zwitter) and of the adopted proper-motion catalogue, and they are exactly what the Jeans equations lead us to expect: V_ϕ decreases as the asymmetric drift increases and the asymmetric drift increases with the velocity dispersion (see e.g. Binney & Tremaine 1998, equation 4.34). In Fig. 11, the velocity dispersion trends in V_ϕ are shown for the RAVE results and the GALAXIA model using the RC-assumption distances. The increase of velocity dispersion with increasing Z and decreasing R is seen in both the data and the model. Consequently, whether we move inwards or away from the plane to regions of increased velocity dispersion, V_ϕ will decrease.

Fig. 8 shows that adopting a different proper-motion catalogue does slightly change the predicted values of V_ϕ: away from the plane slightly higher values of the order of $\Delta \simeq 5-10$ km s^{-1} are
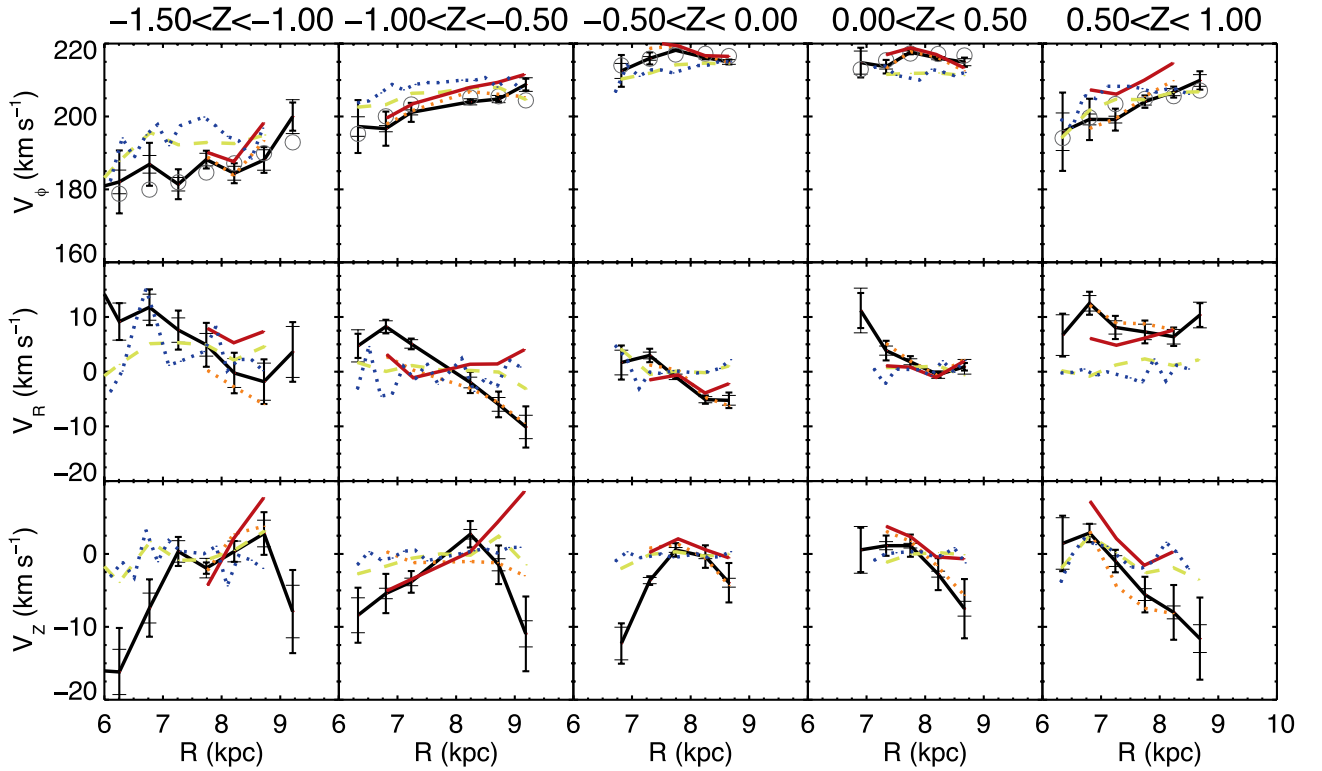
Figure 8. The trends in average velocity as a function of (R, Z) position in the Galaxy for RC stars with RAVE catalogue proper motions (black solid line), UCAC3 proper motions (orange dashed line) and SPM4 proper motions (red dot–dashed line). GALAXIA model results are also given, using the real GALAXIA distances (dark blue) and RC distances (light green). Error bars give the measurement (thick line, short hat) and Poisson (thin line, long hat) errors. The grey open circles in the V_ϕ plot give the result of the fit using RAVE catalogue proper motions in Section 6.1.

obtained with the SPM4 proper motions than those in the RAVE catalogue, while the UCAC3 proper motions give intermediate values ($\Delta \simeq 2-5$ km s^{-1}). However, these differences between results from various proper-motion catalogues are much smaller than the difference between the observations and the predictions of GALAXIA: the latter predicts a markedly flatter profile of V_ϕ with Z. In other words, the data imply that V_ϕ falls away as we move away from the plane significantly more rapidly than GALAXIA predicts. The data give values of V_ϕ 5 km s^{-1} greater than GALAXIA at $Z = 0$ kpc, falling below the model at $|Z| = 0.5$ kpc to be -10 km s^{-1} lower at $|Z| = 1$ kpc.

In Section 4.1.1, we saw that the assumption of a single RC magnitude can lead to an underestimation of V_ϕ by ~ 5 km s^{-1}. This effect is also evident in Fig. 8 in that the dotted green lines obtained for the GALAXIA model using RC distances lie below the dashed

blue lines obtained with the true distances, again by about 5 km s^{-1}. Further, in Section 4.1.2 and Fig. 5, we saw that for large values of Z, M_K normalizations B and C give lower values of V_ϕ as large as 15 km s^{-1}. The effect was only at the extremities of the data however. Since even the green lines lie above the data for $|Z| > 0.5$ kpc, we conclude that the use of a single RC magnitude or the chosen M_K normalization does not explain the offset between the data and the predictions of GALAXIA and the Galaxy's velocity field must differ materially from that input into GALAXIA. Comparison of the top and bottom panels of Fig. 10 reveals that, compared to the predictions of GALAXIA, the observations show more clearly the expected tendency for V_ϕ to decrease as we move in at fixed $|Z|$.

In their study of the HTDC, Parker et al. (2004) measured the line-of-sight velocities of thick-disc and halo stars, finding that in quadrant 1 the rotation of this body of stars lagged the LSR by
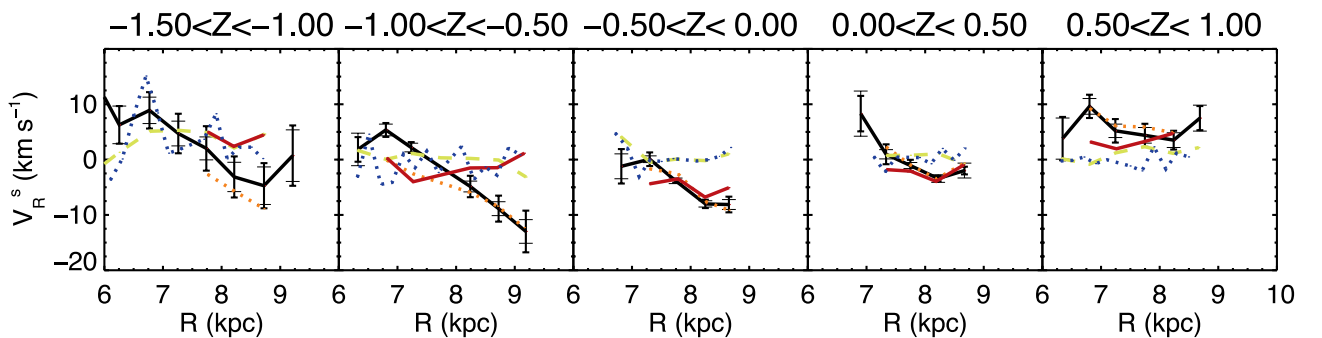

Figure 9. As in Fig. 8 with however V_R^s giving the Galactocentric radial velocity with $U_\odot = 14$ km s^{-1}. The values are shifted down with the overall trends unaffected.
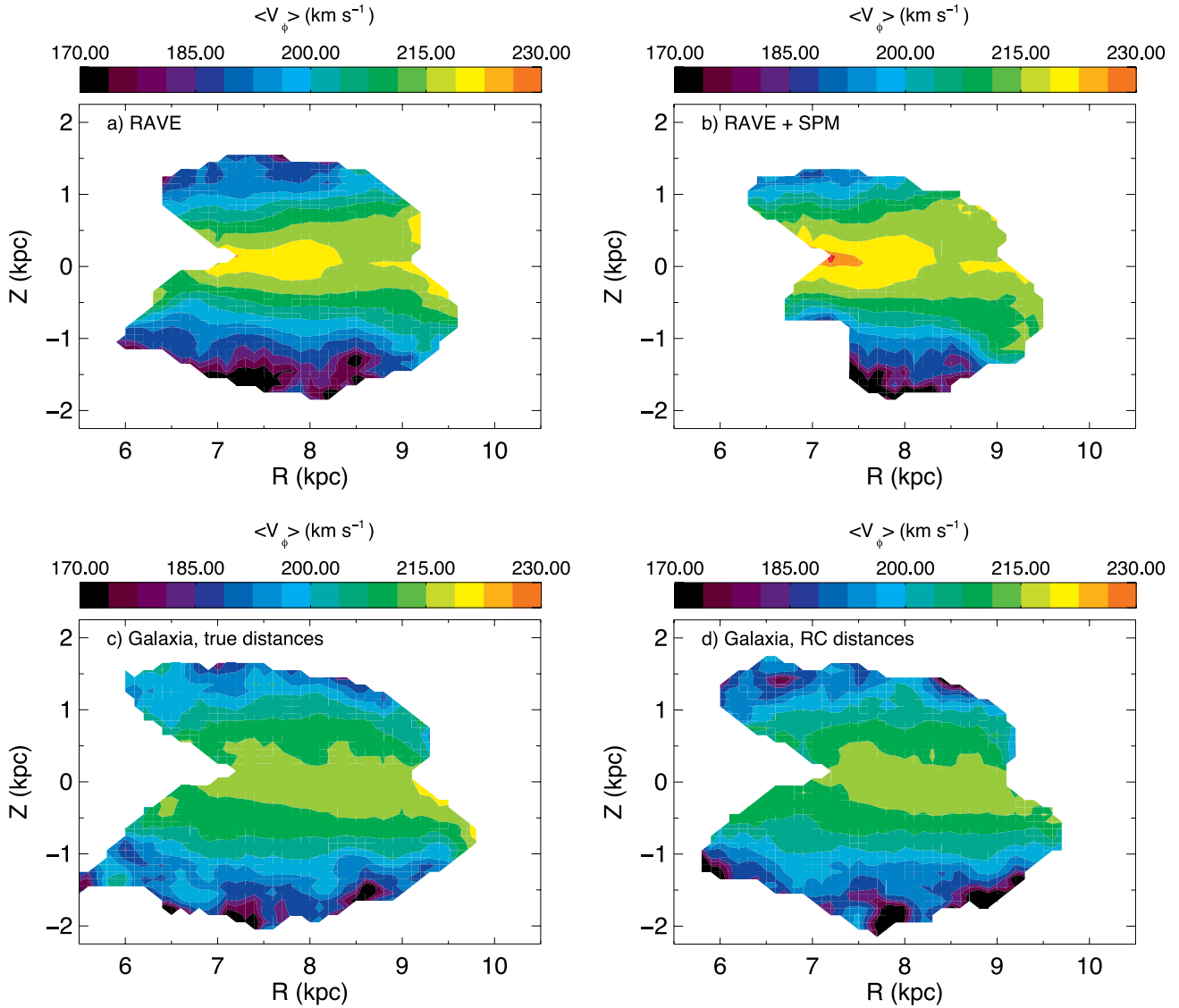
Figure 10. The trends in average V_ϕ as functions of position in the (R, Z) plane for RAVE RC stars with RAVE catalogue proper motions (a) and SPM4 proper motions (b). GALAXIA model results using the 'true' GALAXIA distances (c) and the RC-distances (d) are also presented. The plotted data are box-car averages over 200 pc × 200 pc wide boxes in (R, Z) with 100 pc increments in the coordinates of the box's centre.

80–90 km s^{-1}, while in quadrant 4 the corresponding lag was only 20 km s^{-1}. Far from confirming this effect, the centre-left panel of Fig. 14 suggests if anything the opposite is true: at $X \simeq 1.5$ kpc and $-1 < Z < -0.5$ kpc, V_ϕ is lower in the quadrant 4 than quadrant 1.

The red curves of Fig. 14 show the positions of spiral arms. Close to the plane, at $-0.5 < Z < 0.5$ there is some hint that there is an increasing lag in V_ϕ associated with the spiral features. Further from the plane, such an association is less clear, as one might expect.

The (R, Z) dependence of V_ϕ is best described by the power law:

$$V_\phi = a_1 + \left(a_2 + a_3 \frac{R}{\text{kpc}} \right) \left| \frac{Z}{\text{kpc}} \right|^{a_4} \text{ km s}^{-1} \quad (2)$$

with Table 4 giving the coefficients for the three different proper-motion sources.

The form is not dissimilar to that given for high-metallicity stars in Ivezić et al. (2008) between $2 < R < 16$ kpc and $0 < |Z| < 9$ kpc

($\langle V_Y \rangle = 20.1 + 19.2|Z \text{ kpc}^{-1}|^{1.25}$ km s^{-1}) and Bond et al. (2010) between $0 < R < 20$ kpc and $0 < |Z| < 10$ kpc ($\langle V_\phi \rangle = -205 + 19.2|Z/\text{kpc}|^{1.25}$ km s^{-1}). These results are not directly comparable to our fitting formula as we have an extra component that takes radial R dependence into account, which may lead to interaction between the fit coefficients. Nevertheless, our range of values for the exponent (1.06–1.38) for the vertical Z dependence is similar to their results (1.25).

6.2 V_R

In the top panels of Fig. 12, contours of constant V_R are by no means vertical, whether one adopts the proper motions in the RAVE or SPM4 catalogues. In fact, with the SPM4 proper motions, the contours are not far from horizontal. Thus, the radial gradient $\delta V_R/\delta R = -3$ km s^{-1} kpc^{-1} reported by S11 is at the very least just one aspect of a complex phenomenon. In fact, if the SPM4 proper motions are correct, the trend in V_R is essentially that the
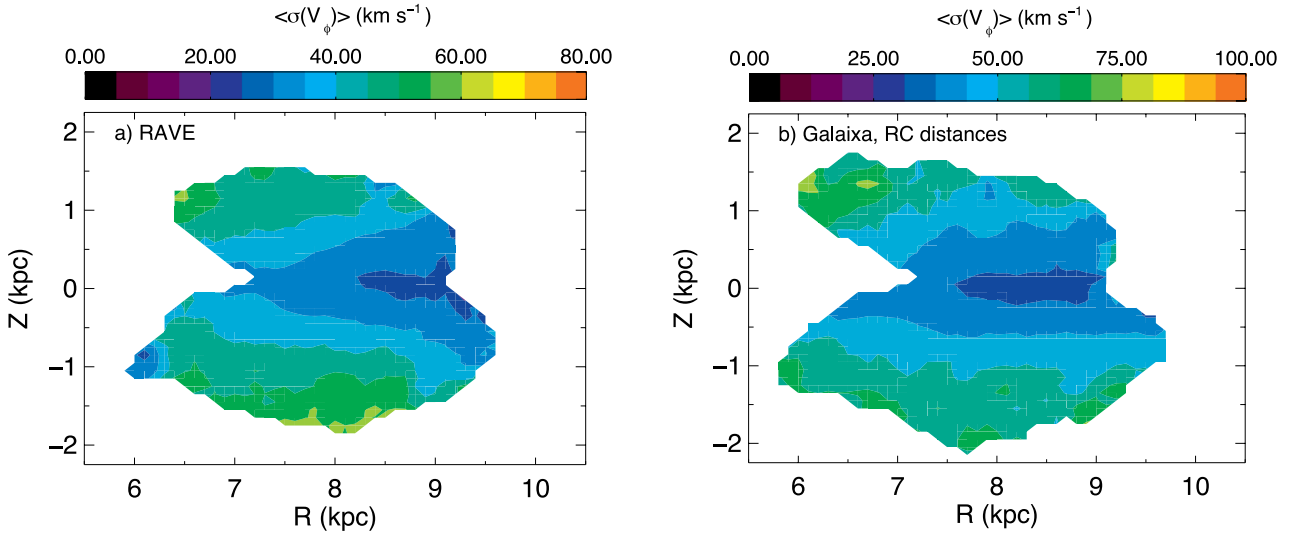
Figure 11. The trends in average $\sigma(V_\phi)$ as functions of position in the (R, Z) plane for RAVE RC stars with RAVE catalogue proper motions (a) and for GALAXIA model results using the RC distance method (b). The velocity dispersion increases as V_ϕ decreases.

Table 4. Parameters for the fit given by equation (2) to the V_ϕ trends using the three proper-motion sources; the RAVE-catalogue compiled results, SPM4 and UCAC3. The ranges of validity in R and Z are also given.

	a_1	a_2	a_3	a_4	Z (kpc)	R (kpc)
RAVE catalogue	225	-51.2	2.6	1.06	$[-1.5, 1.5]$	$[6, 9]$
SPM4	222	-40.2	2.1	1.38	$[-1.5 \ 1.0]$	$[7, 9]$
UCAC3	224	-54.7	3.2	1.10	$[-1.5, 1.0]$	$[7, 9]$

further stars are from the plane, the more they are moving away from the Galactic Centre.

The middle panel of Fig. 8 shows this situation in a different way by showing that the red curves for the SPM4 data are horizontal within the errors at all distances from the plane, but they move down from $V_R \simeq 8 \, \text{km s}^{-1}$ at $Z \simeq -1.25 \, \text{kpc}$ to zero in the plane and back up to $\sim 8 \, \text{km s}^{-1}$ at $Z \sim 0.75 \, \text{kpc}$. In this figure, the black curves that join the RAVE data points tell a different story in that in the panels for $Z \lesssim 0$ they slope firmly downwards to the right. In the two panels for $Z > 0$ the data points from the RAVE proper motions are consistent with no trend in V_R with R with the exception of the innermost point in the panel for $Z \sim 0.25 \, \text{kpc}$, which carries a large error bar. The present analysis is consistent with the value of $\delta V_R / \delta R$ reported by S11 in that $-3 \, \text{km s}^{-1} \, \text{kpc}^{-1}$ is roughly the average of the gradient $\delta V_R / \delta R \simeq -7$ to $-8 \, \text{km s}^{-1} \, \text{kpc}^{-1}$ given by the RAVE proper motions at $Z < 0$ and the vanishing gradient at $Z > 0$.

If the dominant gradient in V_R is essentially in the vertical direction and an even function of Z as the SPM4 proper motions imply, the suspicion arises that it is an artefact generated by the clear, and expected, gradient of the same type that we see in V_ϕ. The gradient could be then seen to be caused by systematics in the proper motions creating a correlation between the measured value of V_R and V_ϕ (see e.g. Schönrich, Binney & Asplund 2012). In Section 7, we re-explore the line-of-sight detection of the V_R, which is a proper-motion-free approach to observing the radial gradient, which however corroborates the existence of a gradient and north–south differences.

Schönrich (2012) found a larger value of $U_\odot = 14 \, \text{km s}^{-1}$ compared to that used in this study and S11, and suggests that this larger value would reduce the gradient in V_R. In Fig. 9, we plot V_R^s, the Galactocentric radial velocity with $U_\odot = 14 \, \text{km s}^{-1}$. The qualitative trends are unaffected by the higher value of $U_\odot$, with the values only shifted down, bringing the values in the $0.5 < Z < 1.0 \, \text{kpc}$ bin closer to those predicted by GALAXIA.

In Fig. 14, the location of the spiral arms is overlaid for reference on the full XYZ plots of V_R trends. There is some indication that structure in V_R is coincident with spiral arms in the $-1.0 < Z < -0.5 \, \text{kpc}$ region, with quadrant 3 and quadrant 4 showing the largest gradient. With a scaleheight of the thin disc of $300 \, \text{pc}$ (Gilmore & Reid 1983), at these large Z values we would not expect however that spiral resonances would play a role. However, the recent results of S12 which explained the gradient in terms of such resonances suggests that they do exert an influence at large distances from the Galactic plane. The diminishment of the gradient at positive Z values is also evident in this figure. Further modelling in 3D is required to understand if the north–south differences in the gradient can be explained in terms of resonances due to spiral structure, which one would expect to produce effects symmetric with respect to Z.

The bottom panels of Fig. 12 shows the corresponding GALAXIA model for the red clump. Here, we see that there is an absence of the observed north–south asymmetry, and further, we confirm that the asymmetry is not produced by using the red-clump distance estimate. We have explored the influence of changing the distances using the Zwitter distances. We found that these alternative distance calculations also show the same overall R, Z variations for V_R, while exhibiting some differences in various regions. This indicates that while the distances may influence the quantitative results, qualitatively the overall trends remain the same.

6.3 V_Z

The top panels of Fig. 13 show that both proper-motion catalogues yield a similar dependence of V_Z on (R, Z). We see a ridge of enhanced V_Z that slopes across the panel, making an angle of
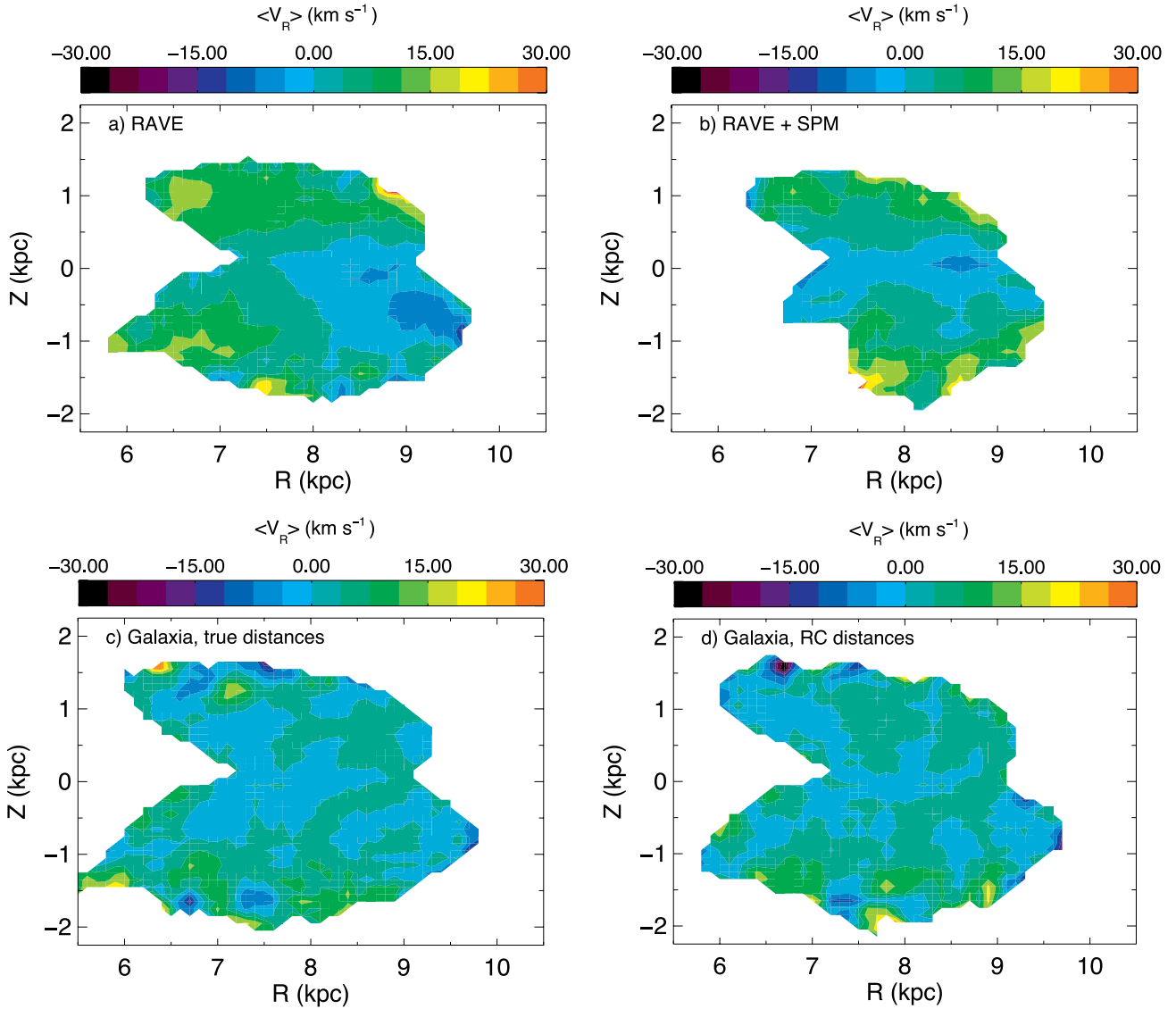
Figure 12. As in Fig. 10, but for V_R.

approximately $40°$ with the R-axis and cutting that axis about 0.5 kpc outside the solar radius. This feature is most pronounced in the bottom-left panel, for proper motions in the RAVE catalogue. If we assume the LSR V_Z value is zero, and thus the top of the ridge has $V_Z = 0$, we could interpret the stars interior to this point showing an overall rarefaction: stars below the plane move downwards, while those above the plane, move upwards. Exterior to $R = 8.5$ kpc the behaviour is reversed and shows a compression; below the plane stars move upwards, while above the plane stars move downwards. The amplitude of these variations is large, up to $|V_Z| = 17$ km s^{-1} as seen from Fig. 8.

The results for the SPM4 and UCAC3 proper motions do not exhibit quite so large an amplitude in the V_Z variations, but as shown in Fig. 13 for SPM4, exhibit a similar overall behaviour, with the line of higher V_Z running diagonal across the RZ plane. However, in Fig. 8 we see that below the plane, the alternative proper-motion results do not show the large dip in V_Z at $R = 9$ kpc, though this is mostly due to the smaller sampling area in the XY plane of the alternative proper-motion sources. Above the plane, the

behaviour of the results from the various proper-motion sources is similar, with clear deviation from the GALAXIA model's predictions in the bottom panels of Fig. 13. The GALAXIA model itself shows a random pattern of high and low V_Z of the order of 5 km s^{-1}. There is some smoothing spatially of these fluctuations with the use of RC-magnitude-derived distances, though the observed pattern is not generated with this distance method. In general, the proper motions dominate the calculated V_Z values, and the differences in observed structure reflect this. Nonetheless, it is reassuring that the overall pattern is recovered in Fig. 13 with each proper-motion catalogue source.

Recently, Widrow et al. (2012) found with main-sequence Sloan Digital Sky Survey (SDSS) stars that the vertical number-density and V_Z profiles suggest vertical waves in the Galactic disc excited by a recent perturbation. A direct comparison with their results and ours is not possible as their stars are outside the RAVE spatial sampling region. However, our results support this proposition: the rarefaction and compression behaviour seen in the top panels of Fig. 13 is indicative of wave-like behaviour. This could then be seen as further
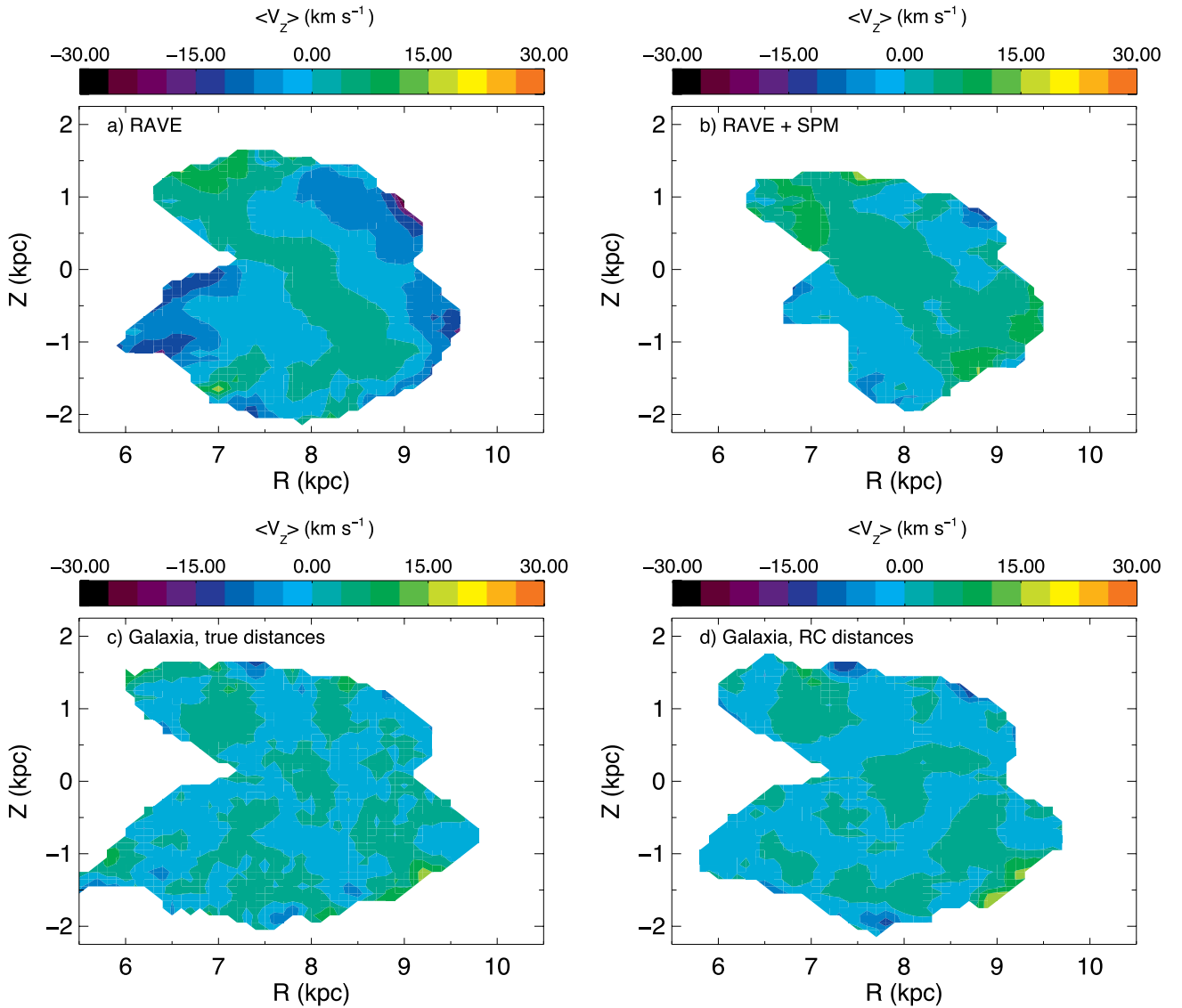
Figure 13. As in Fig. 10, but for V_Z.

'ringing' behaviour of the disc caused by a recent accretion event, as in Minchev et al. (2009) and Gómez et al. (2012a). Indeed, Gómez et al. (2013) further suggest that such vertical waves may have been excited by the Sagittarius dwarf as it passed through the disc. Their simulations find deviations of up to 8 km s^{-1} in V_Z in a heavy-Sgr scenario.

Turning now to Fig. 14 we find some suggestion that the V_Z field shows some alignment with spiral-arms feature, even at significant distances from the plane. Below the plane, the Sagittarius–Carina arm at $X \sim 1.5$ kpc is aligned with the low V_Z velocities seen with the RAVE catalogue proper motions for $Y < 0$. In this representation, the SPM4 and UCAC3 proper-motion results also show a dip in their V_Z velocities around this area, though the feature is not as pronounced as for the RAVE catalogue proper motions. The Perseus arm is also aligned with an area of lower V_Z at $X = -1.25, Y < 0, Z < -0.5$ kpc. Across all values of Z, the alignment of the V_Z features with the spiral arms is less clear for $Y > 0$, which below the plane may be explained by the proximity of the HTDC. S12 showed how spiral

density waves could be used to explain the V_R streaming motion. Siebert et al. (in preparation) goes further to investigate how they could also create the V_Z structures, coupled to V_R.

These results suggest that there are large-scale vertical movements of stars, with various cohorts at the same Z moving in opposing directions. In Casetti et al. (2011), it was proposed that while the Galactic warp starts at the solar radius, the small elevations of the warp at these distances (70−200 pc for $R = 8$−10 kpc (López-Corredoira et al. 2002)) and the large distances of the RAVE stars from the plane would mean that kinematics of stars would be little affected by the warp. In Russiel (2002), the nearby Sagittarius–Carina arm as traced by star-forming complexes is found to lie mostly below the plane by 100−200 pc, which suggests that nearby spiral arms can be influenced by some warping. Whether the warp is long-lived or a transient feature would have implications for the associated velocities. The complexity of the vertical velocity distribution suggested by our results would tend to point towards transient features: they suggest a non-equilibrium state. A multimode
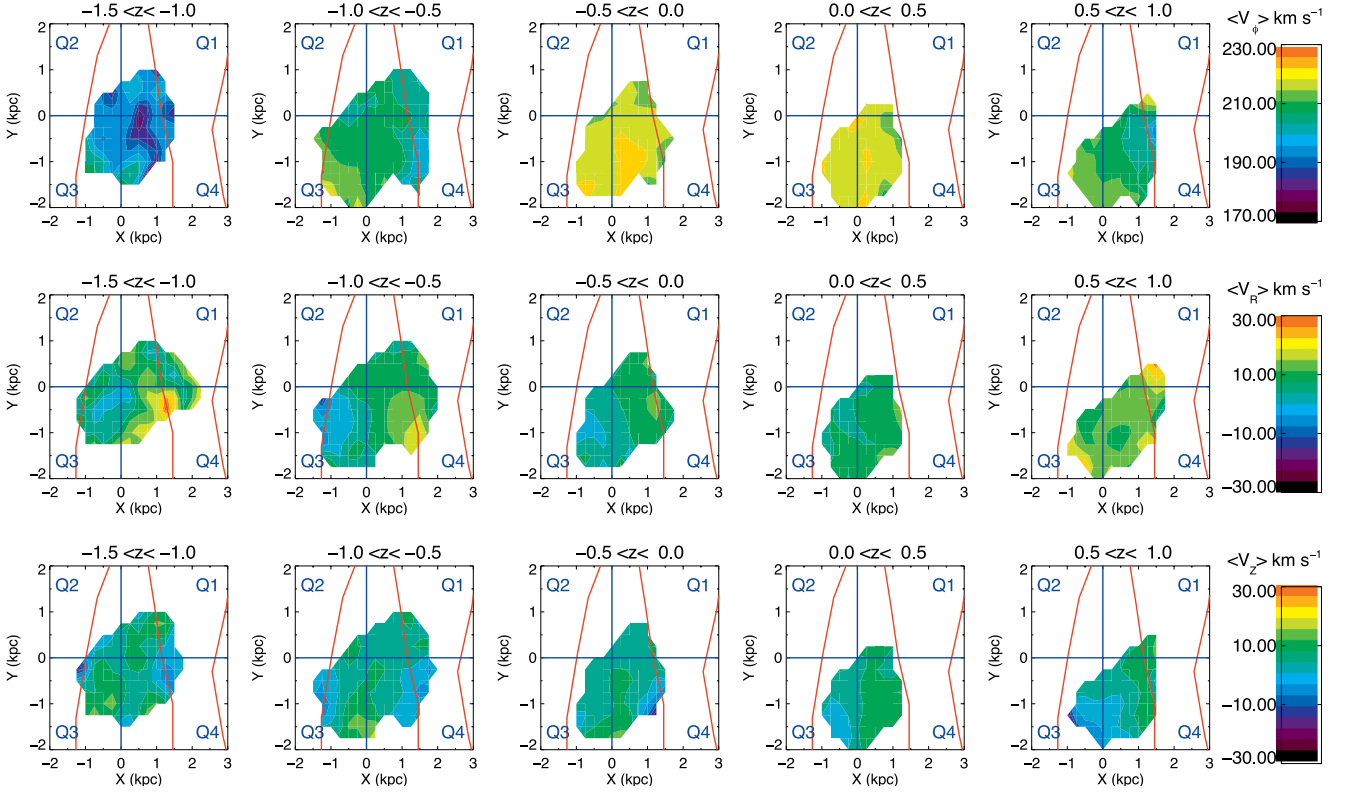
Figure 14. The trends in average V_ϕ (top), V_R (middle) and V_Z (bottom) as a function of (X, Y, Z) position in the Galaxy for RC stars only using RAVE catalogue proper motions. The position of the spiral arms (red lines) are also plotted.

travelling wave caused by a recent accretion event, or structure associated with the disc's spiral arms, would be the most likely explanations for the observed velocity structure.

6.4 Velocity dispersion trends

The second moments of the velocity components increase with increasing Z and decreasing R in a smooth fashion as expected, with Fig. 11 showing the results for $\sigma(V_\phi)$. As for V_ϕ, they can be fit by a simple parametric function.

Fig. 15 displays the trends in the dispersion of V_ϕ, V_R, V_Z as a function of Z for 0.5 kpc thick slices in R using 0.5 kpc bins in Z. Also plotted are the results based on UCAC3 and SPM4 proper motions, and the GALAXIA model results using the 'true' model distances plus RC-calculated distances. Unlike the mean-value trends, the differences between the various proper-motion sources is minimal. We see however that the GALAXIA model results indicate that the use of RC-calculated distances can lead to an increase in the measured dispersion values, particularly for V_R. Interestingly however, there is reasonable agreement between the results of GALAXIA and that observed with RAVE.

We note that the dispersions were corrected for errors following the same methodology of Casetti et al. (2011). This method adjusts a guess of the true dispersion, σ_V, in velocity component V until

$$\text{stddev}((V_i - \bar{V})/\sigma_T) = 1 \qquad (3)$$

where $\sigma_T^2 = \sigma_V^2 + eV_i^2$, with eV_i the MC-derived error in V for ith star and $\bar{V} = \text{mean}(V_i)$ is the mean over the sample.

The velocity dispersions exhibit linear behaviour in R and parabolic behaviour in Z. Thus, a fit to the dispersion trends was found to be provided by the simple form

$$\sigma_V = b_1 + b_2 \frac{R}{\text{kpc}} + b_3 \frac{Z}{\text{kpc}}^2 \text{ km s}^{-1} \qquad (4)$$

with Table 5 giving the coefficients for the three velocity components for the three different proper-motion sources. The similar coefficients for each velocity component underlines the similarity of the trends between the three sources.

7 VELOCITY GRADIENT: LINE-OF-SIGHT DETECTION

In S11, the gradient in V_R was first investigated using the line-of-sight velocity, V_{los}, along narrow lines towards the centre and anticentre. The rationale for this approach was to observe the V_R gradient independent of the proper motions. The complicated 3D structure of the Galactic V_R profile was not considered so we revisit this approach, keeping in mind the 3D trends.

7.1 V_R

Fig. 3 from S11 gives the projection on to the plane of the mean V_{los} in bins 200 pc wide as a function of $d \cos l \cos b$, with the latter a proxy for X in their Galactic coordinates, with $X_{\text{S11}} \sim R_\odot - d \cos l \cos b$. For $|l| < 5°$ and $175° < l < 185°$, the values of the radial component, V_R, are essentially the same as the Cartesian value $-U$. As most stars in these narrow cones have $\cos b/\sin b \sim 1.5$, U (and so $-V_R$) is dominated by the term $V_{\text{los}} \cos b$. In the appendix, we list the relevant equations which shows how this follows. S11b
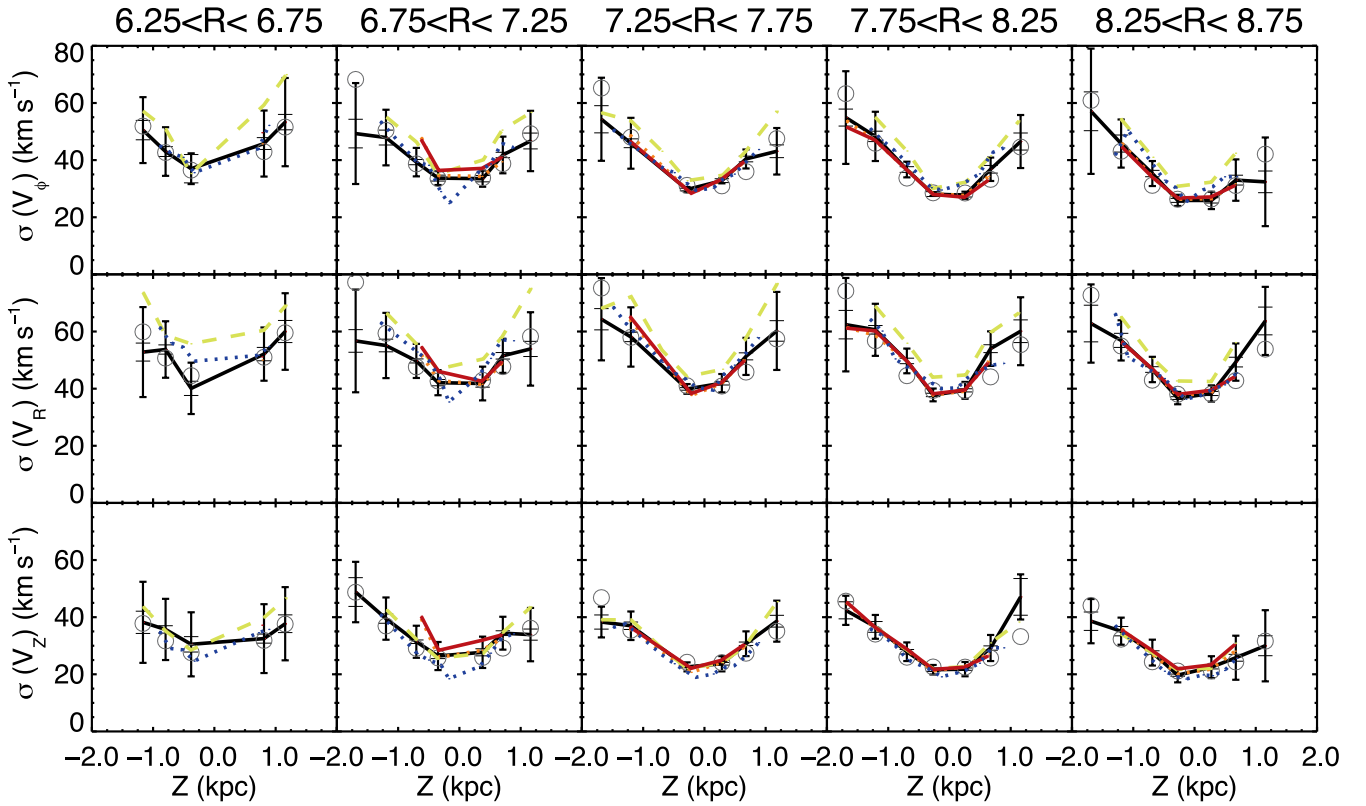
Figure 15. The trends in velocity dispersion as a function of (R, Z) position in the Galaxy for RC stars with RAVE catalogue proper motions (black solid line), UCAC3 proper motions (orange dashed line) and SPM4 proper motions (red dot–dashed line). GALAXIA model results are also given, using the real GALAXIA distances (dark blue) and RC distances (light green). Error bars give the measurement (thick line, short hat) and Poisson (thin line, long hat) errors. The open circles give the results of the fitting formula using the coefficients from the RAVE catalogue proper motions fit.

compared the mean velocities to those expected for a thin disc in circular rotation and adding a radial gradient of $\partial(V_R)/\partial R = -3, -5$ and $-10\,\mathrm{km\,s^{-1}\,kpc^{-1}}$ (plus a thick disc lagging the LSR by $36\,\mathrm{km\,s^{-1}}$), finding that the results were consistent with a radial gradient of $\partial(V_R)/\partial R = -3$ to $-5\,\mathrm{km\,s^{-1}\,kpc^{-1}}$.

From equations (A1) and (A7) in the appendix, we see that if we are to consider the V_{los} as representative of U (and so $-V_R$),

Table 5. Parameters for the fit given by equation (4) to the velocity dispersion trends using the three proper-motion sources; the RAVE-catalogue compiled results, SPM4 and UCAC3. The parameters are valid for the same ranges given in Table 4.

	b_1	b_2	b_3
V_ϕ			
RAVE catalogue	67.4	−5.0	12.4
SPM4	75.7	−6.1	15.8
UCAC3	71.2	−5.5	15.2
V_R			
RAVE catalogue	62.6	−3.0	12.5
SPM4	60.0	−2.7	15.1
UCAC3	63.3	−3.1	13.5
V_Z			
RAVE catalogue	47.0	−3.1	8.2
SPM4	49.4	−3.4	9.8
UCAC3	43.6	−2.8	10.4

technically it would be better to first subtract the solar motion from the line-of-sight velocity, to obtain V'_{los}. Otherwise the components above and below the plane will be shifted from each other, which can be problematic if the sample shifts from above-the-plane to below-the-plane, potentially producing spurious trends. This was omitted in the analysis of fig. 3 from S11; however, it did not affect the conclusions as the models were similarly shifted.

In Fig. 16, we re-examine the trends in $V_{\mathrm{los}} \cos b$ for the RC giants and stars with Zwitter distances, where we plot against R rather than $d \cos l \cos b$ as this is easier to interpret and there is little difference between the two values. We plot the results with and without the LSR correction, with the curve being flattened in the latter with the removal of the $U_\odot$ component. We also plot the trends for a thin disc as in S11, using 100 Monte Carlo realizations. We see here that not correcting for the solar motion does not affect the conclusions. Note that with the updated data sets the V_R streaming motion is slightly less apparent in both the RC and Zwitter results than it was in S11: the model with $\partial(V_R)/\partial R = -3\,\mathrm{km\,s^{-1}\,kpc^{-1}}$ is a better fit to the data. Also, the differences between the RC and Zwitter trends around the solar radius in Fig. 16 is a result of the different geometric sampling of the two.

In Fig. 17, we examine the $V'_{\mathrm{los}} \cos b$ results split into north and south components. In this we open up the criteria a bit to within 7° of the centre and anticentre direction to reduce the effects of Poisson noise and make the trends clearer. Here, we see that differences can be discerned between the north and south trends; however, they are opposite to that seen in the previous section; the gradient in the north (-5 to $-10\,\mathrm{km\,s^{-1}\,kpc^{-1}}$) is stronger though absent in the south ($0\,\mathrm{km\,s^{-1}\,kpc^{-1}}$) for $R < 8\,\mathrm{kpc}$. Plotting the corresponding
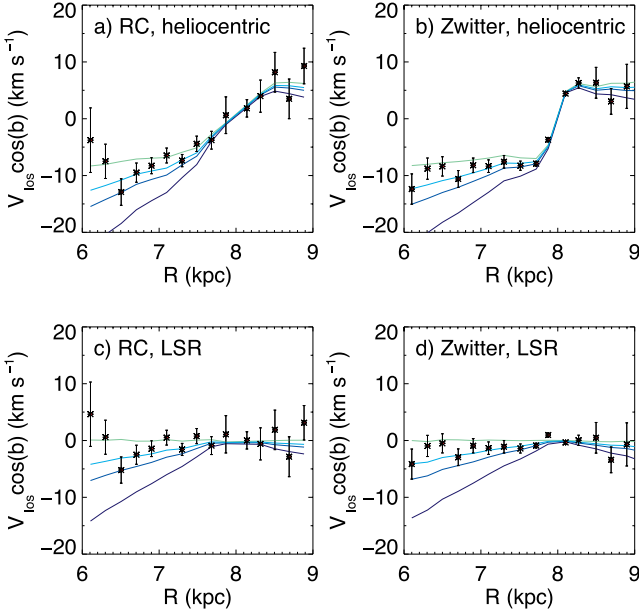
Figure 16. As in fig. 3 of S11, projection of mean RAVE V_{los} on the Galactic plane in distance intervals of 200 pc towards the Galactic Centre ($|l| < 5°$) and anticentre ($175° < l < 185°$). Panels (a) and (c) show the results for RC stars with heliocentric line-of-sight velocity and corrected to the LSR, respectively, while (b) and (d) similarly show the Zwitter distance results. The solid curves represent a thin-disc population with a radial velocity gradient of $\delta V_R/\delta R = 0, -3, -5$ and -10 km s^{-1} kpc^{-1}, going from green to purple.
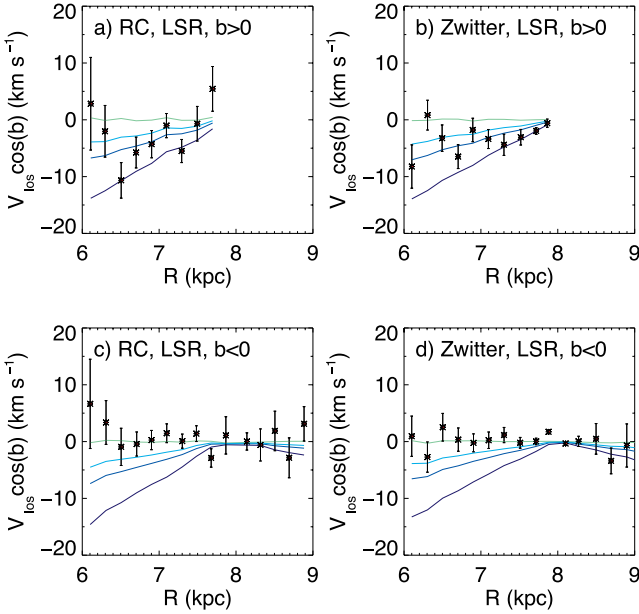
Figure 17. As in the bottom plots of Fig. 16, but for Galactic Centre ($|l| < 7°$) and anticentre ($173° < l < 187°$) and split into above (a, b) and below (c, d) the plane.

results for V_R in Fig. 18, we find that the including the proper-motion results shifts the overall values so that the northern trends are more in line with $\delta V_Z/\delta R = -10$ km s^{-1} kpc^{-1} and the southern $\delta V_Z/\delta R = -3$ to -5 km s^{-1} kpc^{-1}. Despite the disparity with the actual numbers, the cause of which is discussed below, both
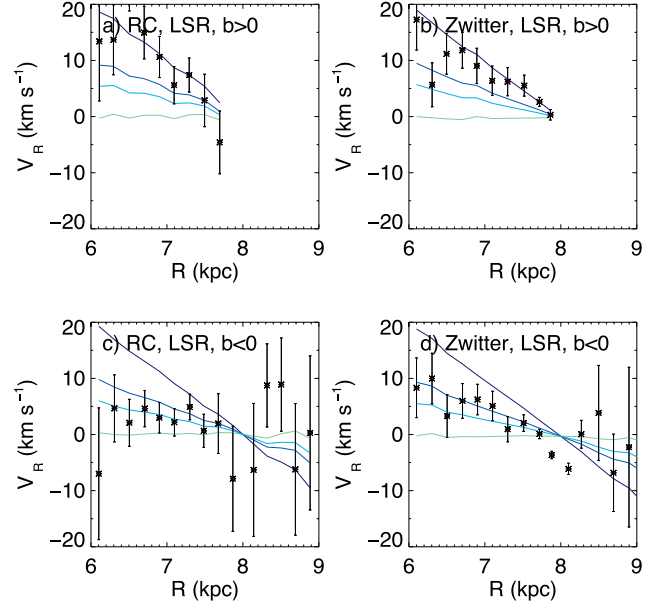

Figure 18. Corresponding V_R trends to Fig. 17, looking at the Galactic Centre ($|l| < 7°$) and anticentre ($173° < l < 187°$) and split into above (a, b) and below (c, d) the plane.

$V'_{los} \cos b$ and the V_R nonetheless exhibit differences between the north and south trends, opposite to those found in Section 6.2.

To understand the reversal of the trends note first that the selected sample cuts across a range of Z as we change R so these plots combine the R and Z trends seen previously. Secondly, the necessary restriction on l means that we are sampling a very narrow beam and thus do not see the global patterns, but only those along that beam. In Fig. 14, quadrants 3 and 4 show the largest gradient, which we miss with the beams. Hence, these plots emphasize the 3D nature of the V_R values in the solar neighbourhood: what you measure very much depends on where you look, be it north or south, and at different R and Z values.

7.2 V_Z

From equation (A6) in the appendix, we can see that $V'_b \cos b$ can be used as a proxy for $W = V_Z$ if $|\cos b| > |\sin b|$. This condition is for the most part met in the low latitudes sampled along the $|l| < 7°$ and $173° < l < 187°$ cones used above. So in Fig. 19, we examine the trends above and below the plane for $V'_b \cos b$ in these directions, with Fig. 20 giving the corresponding trends in the total V_Z. Note that we use RC and Zwitter distances here to provide the abscissa, supplementing the proper-motion data. We also plot both positive and negative trends in V_Z for a thin-disc model as above, with values from $\partial(V_Z)/\partial R = -10, -5, -3, 0, 3, 5, 10$ km s^{-1} kpc^{-1}.

Both Figs 19 and 20 show that the trends above and below the plane are markedly different, with the V_Z decreasing with R above the plane at a rate of $\partial(V_Z)/\partial R \sim -10$ km s^{-1} kpc^{-1} according to the $V'_b \cos b$ plot and -5 km s^{-1} kpc^{-1}, to the V_Z plot. Below the plane, there is a positive trend of $\partial(V_Z)/\partial R \sim +5$ km s^{-1} kpc^{-1} in both plots. This positive trend in V_Z appears to stop just beyond the solar circle at $R \sim 8.5$ kpc. In contrast to V_R above, this behaviour is consistent with what was found in Section 6.3.

Note that the differences between the observed magnitude of the trends in $V'_{los} \cos b$ and V_R, plus $V'_b \cos b$ and V_Z can be explained by the fact that both V'_{los} and V'_b contain components of
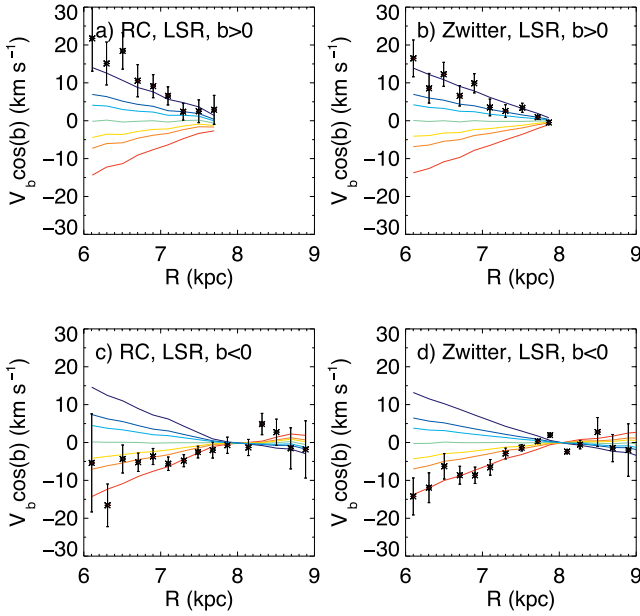
Figure 19. $V_b' \cos b$ for Galactic Centre ($|l| < 7°$) and anticentre ($173° < l < 187°$) directions and split into above (a, b) and below (c, d) the plane. The solid curves represent a thin-disc population with a radial velocity gradient of $\delta V_Z/\delta R = 10, 5, 3, 0, -3, -5$ and $-10 \, \mathrm{km \, s^{-1} \, kpc^{-1}}$, going from red to green to purple.
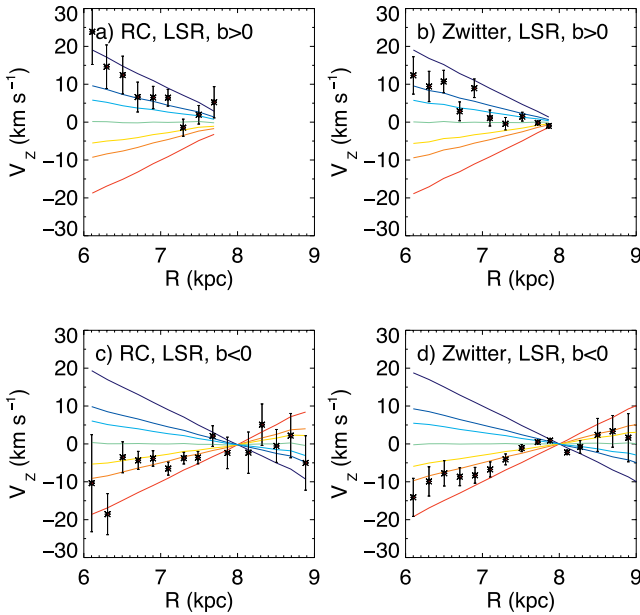

Figure 20. Corresponding V_Z trends to Fig. 19, looking at the Galactic Centre ($|l| < 7°$) and anticentre ($173° < l < 187°$) directions and split into above (a, b) and below (c, d) the plane.

U and W. For small l, $V_{\mathrm{los}}' \cos b = U' \cos^2 b + W' \cos b \sin b$ and $V_b' \cos b = -U' \sin b \cos b + W' \cos^2 b$. The cross-terms mean that there is some 'leakage' of the V_Z trends into $V_{\mathrm{los}}' \cos b$ and V_R trends into $V_b' \cos b$, which work to either diminish or enhance the observed trend in the single component. Nonetheless, the fact that there *are* differences between the north and south for the single components at all is further evidence of the 3D variations of the velocity values.

The V_R and V_Z trends, as seen via the line-of-sight velocities and proper motions, respectively, are unaffected by potential systematics

in the distances: a change of the distance scale would not affect the fact that a trend is seen at all. This is particularly so for the differences observed between the northern and southern samples. Furthermore, both the SPM and UCAC3 proper motions give similar results as in Fig. 19, with a stark negative trend above the plane and a positive trend below for the region $R < 8.5$ kpc. Thus, neither the distances nor the proper motions introduce large systematics into this method of detection.

8 CONCLUSION

Using RAVE red-clump giants, we have examined in detail the first moments of the velocity components in a large volume around the Sun. We find differences between the north and south in the streaming motion reported in S11 in Galactocentric radial velocity, V_R. Above the plane, there is a large outward flow ($V_R = 8-10 \, \mathrm{km \, s^{-1}}$ for $0 < Z < 1$ kpc) with a shallow or non-existent gradient. Below the plane, there are lower values of V_R outside the solar circle, down to $V_R = -10 \, \mathrm{km \, s^{-1}}$ at $R = 9$ kpc, $-1 < Z < -0.5$ kpc. This is associated with a much steeper gradient in R, particularly in quadrants 3 and 4, the largest gradient being $\delta V_R/\delta R = -8 \, \mathrm{km \, s^{-1} \, kpc^{-1}}$ for $-1 < Z < -0.5$ kpc.

The behaviour of V_Z shows a surprising complexity suggestive of a wave of compression and rarefaction: there is a ridge of higher V_Z passing at an angle of $40°$ to the plane, intersecting the plane just outside the solar circle. Assuming the LSR V_Z to be zero, stars interior to the solar circle and above the plane are moving upwards, while those below the plane, downwards. Exterior to the solar circle, stars both above and below are moving on average towards the plane. Values of up to $|V_Z| = 17 \, \mathrm{km \, s^{-1}}$ are observed. We confirm these differences by examining the transverse velocities along narrow cones towards and away-from the Galactic Centre.

Physically, the V_Z velocity field implies alternate rarefaction and compression, as in a sound wave. Thus, our three-dimensional velocity field confirms the recent one-dimensional results of Widrow et al. (2012) in which north–south differences in the velocities of SDSS stars suggested vertical waves in the Galactic disc. Two likely causes of these waves are either a recently accreted satellite or the disc's spiral arms. Further modelling will hopefully help decide between these two scenarios.

V_ϕ is much more regular than the other two components, showing the most qualitative agreement with the mock sample created with the GALAXIA model for the Galaxy and the expected increase of V_ϕ with increasing Z and decreasing R. The model gives a much flatter profile of V_ϕ with Z however than the data; at $Z = 0$ kpc we measure V_ϕ values $5 \, \mathrm{km \, s^{-1}}$ larger than GALAXIA, falling to $-10 \, \mathrm{km \, s^{-1}}$ lower at $|Z| = -1$ kpc. There is some hint of an increased lag in V_ϕ near the plane associated with spiral arm features. We present a simple parametric fit to the V_ϕ dependence on R and Z.

We also trace the second moments of the velocities as a function of R and Z, providing a simple parametric fit to these trends as well.

The red clump is increasingly being used as a standard candle for field stars, given its ease of identification and the relative insensitivity of the M_K magnitude to age and metallicity. We modelled our selection of RC stars using GALAXIA, showing a surprisingly high level of contamination by first-ascent giants despite a tight selection in the $\log g$–$(J - K)$ plane. However, given that the majority of these giants have a similar magnitude to the red clump itself, the effect on the distances does not render them unusable. It means though that there is further complexity in the metallicity–age mixture of selected red-clump stars: the population is by no means homogenous in age and abundance.

The assumption of a single M_K magnitude for the RC and the proper motions are the largest sources of systematic error in our analysis. Indeed, a deeper study into proper-motion differences is required to establish which of the catalogues is most trustworthy. Nevertheless, we have established that north–south differences do exist in V_R and V_Z despite these problems. For V_R, a line-of-sight detection, which excludes the proper motions, shows gradients above and below the plane despite the pencil beams in this analysis pointing away from the area of the largest gradient in quadrants 3 and 4. These results particularly illustrate the 3D nature of the velocity field. For V_Z, results using the three proper-motion sources give the same rarefaction–compression behaviour, albeit with some variation in the details.

The 3D structure in V_R and V_Z presents challenges to future modelling of the Galactic disc under the influence of the bar, spiral features and any other perturbations (be they temporally localized or not). It is not intrinsically clear indeed if the structure in the two are coupled or arise from different physical mechanisms.

ACKNOWLEDGEMENTS

REFERENCES

Alonso A., Arribas S., Martinez-Roger C., 1996, A&A, 313, 873
Alves D. R., 2000, ApJ, 539, 732
Antoja T., Valenzuela O., Pichardo B., Moreno E., Figueras F., Fernández D., 2009, ApJ, 700, 78
Antoja T. et al., 2012, MNRAS, 426, 1
Beers T. C., Chiba M., Yoshii Y., Platais I., Hanson R. B., Fuchs B., Rossi S., 2000, AJ, 119, 2866
Bessell M. S., Brett J. M., 1989, in Milone E. F., ed., Lecture Notes in Physics, Vol. 341, Infrared Extinction and Standardization. Springer-Verlag, Berlin, p. 61
Binney J., Tremain S., 1998, Galactic Dynamics. Princeton Univ. Press, Princeton, NJ
Boeche C. et al., 2011, AJ, 142, 193
Bond N. A. et al., 2008, ApJ, 684, 287
Bond N. A. et al., 2010, ApJ, 716, 1
Burnett B. et al., 2011, A&A, 532, 113
Cannon R. D., 1970, MNRAS, 150, 111
Carpenter J., 2003, Based on Carpenter 2001, ApJ, 121, 2851
Casetti-Dinescu D. I., Girard T. M., Korchagin V. I., van Altena W. F., 2011, ApJ, 728, 7
Chakrabarty D., 2007, A&A, 467, 145
De Silva G. M., Freeman K. C., Bland-Hawthorn J., Asplund M., Bessell M. S., 2007, AJ, 133, 694
De Simone R., Wu X., Tremaine, 2004, MNRAS, 350, 627
Dehnen W., 1998, AJ, 115, 2384

Dehnen W., 1999, ApJ, 524, 35
Englmaier P., Pohl M., Bissantz N., 2008, Mem. Soc. Astron. Ital., preprint (arXiv:0812.3491)
Famaey B., Pont F., Luri X., Udry S., Mayor M., Jorissen A., 2007, A&A, 461, 957
Gilmore G., Reid N., 1983, MNRAS, 202, 1025
Girard T. M. et al., 2011, AJ, 142, 15
Gómez F. A., Minchev I., Villalobos Á., O'Shea B. W., Williams M. E. K., 2012a, MNRAS, 419, 2163
Gómez F. A. et al., 2012b, MNRAS, 423, 3727
Gómez F. A., Minchev I., O'Shea B. W., Beers T. C., Bullock J. S., Purcell C. W., 2013, MNRAS, 429, 159
Grocholski A. J., Sarajedini A., 2002, AJ, 123, 1603
Groenewegen M. A. T., 2008, A&A, 488, 935
Helmi A., White S. D. M., de Zeeuw P. T., Zhao H., 1999, Nat, 402, 53
Humphreys R. M., Beers T. C., Cabanela J. E., Grammer S., Davidson K., Lee Y. S., Larsen J. A., 2011, AJ, 141, 131
Ibata R. A., Gilmore G., Irwin M. J., 1994, Nat, 370, 194
Jurić M. et al., 2008, ApJ, 673, 864
Kazantzidis S., Bullock J. S., Zentner A. R., Kravtsov A. V., Moustakas L. A., 2008, ApJ, 688, 254
Kordopatis G., Recio-Blanco A., de Laverny P., Bijaoui A., Hill V., Gilmore G., Wyse R. F. G., Ordenovic C., 2011, A&A, 535, A106
Kordopatis G. et al., 2013, AJ, in press
Larsen J. A., Humphreys R. M., 1996, ApJ, 468, L99
Larsen J. A., Humphreys R. M., Cabanela J. E., 1996, ApJ, 468, L99
Larsen J. A., Cabanela J. E., Humphreys R. M., 2011, ApJ, 141, 130
López-Corredoira M., Cabrera-Lavers A., Garzón F., Hammersley P. L., 2002, A&A, 394, 883
Majewski S. R., Skrutskie M. F., Weinberg M. D., Ostheimer J. C., 2003, AJ, 599, 182
Matijevič G. et al., 2010, AJ, 140, 184
Matijevič G. et al., 2011, AJ, 141, 200
Matijevič G. et al., 2012, ApJS, 200, 14
Minchev I., Quillen A. C., Williams M., Freeman K. C., Nordhaus J., Siebert A., Bienaymé O., 2009, MNRAS, 396, 56
Minchev I., Boily C., Siebert A., Bienayme O., 2010, MNRAS, 407, 2122
Momany Y., Zaggia S., Gilmore G., Piotto G., Carraro G., Bedin L. R., de Angeli F., 2006, A&A, 451, 515
Newberg H. J. et al., 2002, ApJ, 569, 245
Parker J. E., Humphreys R. M., Larsen J. A., 2003, AJ, 126, 1346
Parker J. E., Humphreys R. M., Beers T. C., 2004, AJ, 127, 1567
Pasetto S. et al., 2012a, A&A, 547, 70
Pasetto S. et al., 2012b, A&A, 547, 71
Peñarrubia J. et al., 2005, ApJ, 626, 128
Pietrzyński G., Gieren W., Udalski A., 2003, AJ, 125, 2494
Pompéia L. et al., 2011, MNRAS, 415, 1138
Quillen A. C., Minchev I., 2005, AJ, 130, 576
Quillen A. C., Dougherty J., Bagley M. B., Minchev I., Comparetta J., 2011, MNRAS, 417, 762
Raboud D., Grenon M., Martinet L., Fux R., Udry S., 1998, A&A, 335, 61
Roeser S., Demleitner M., Schilbach E., 2010, AJ, 139, 2440
Röser S., Schilbach E., Schwan H., Kharchenko N. V., Piskunov A. E., Scholz R.-D., 2008, A&A, 488, 401
Russiel D., 2002, A&A, 397, 133
Salaris M., Girardi L., 2002, MNRAS, 337, 332
Schlegel D. J., Finkbeiner D. P., Davis M., 1998, ApJ, 500, 525
Schönrich R., 2012, MNRAS, 427, 274
Schönrich R., Binney J., Dehnen W., 2010, MNRAS, 403, 1829
Schönrich R., Binney J., Asplund M., 2012, MNRAS, 420, 1281
Sharma S., Bland-Hawthorn J., Johnston K., Binney J. J., 2011, ApJ, 730, 3
Siebert A. et al., 2011a, MNRAS, 412, 2026 (S11)
Siebert A. et al., 2011b, AJ, 141, 187
Siebert A. et al., 2012, MNRAS, 425, 2335 (S12)
Skuljan J., Cottrell P. L., Hearnshaw J. B., 1997, ESASP, 402, 525
Steinmetz M. et al., 2006, AJ, 132, 1645

Tonry J., Davis M., 1979, AJ, 84, 1511

Vallenari A., Pasetto S., Bertelli G., Chiosi C., Spagna A., Lattanzi M., 2006, A&A, 451, 125

van Helshoecht V., Groenewegen M. A. T., 2007, A&A, 463, 559

van Leeuwen F., 2007, Astrophysics and Space Science Library, Vol. 350, Hipparcos, the new reduction of the Raw Data. Springer, Berlin

Widrow L. M., Gardner S., Yanny B., Dodelson S., Chen H., 2012, ApJ, 750, 41

Williams M. E. K. et al., 2011, ApJ, 728, 102

Yanny B. et al., 2003, ApJ, 588, 824

Yasuda N., Fukugita M., Schneider D. P., 2007, AJ, 134, 698

Zacharias N., Urban S. E., Zacharias M. I., Wycoff G. L., Hall D. M., Monet D. G., Rafferty T. J., 2004, AJ, 127, 3043

Zacharias N. et al., 2004, AJ, 139, 2184

Zwitter T. et al., 2008, AJ, 136, 421

Zwitter et al., 2010, A&A, 522, 54

APPENDIX A

The peculiar motion of the Sun is given in the Cartesian values $(U_\odot, V_\odot, W_\odot)$. We define the line-of-sight velocity and proper-motion vectors in (l, b) coordinates corrected for reflex of the solar motion:

$$V'_{\mathrm{los}} = V_{\mathrm{los}} + (U_\odot \cos l \cos b + V_\odot \sin l \cos b + W_\odot \sin b), \quad (A1)$$

$$V'_l = V_l + (-U_\odot \sin l + V_\odot \cos l), \quad (A2)$$

$$V'_b = V_b + (-U_\odot \cos l \sin b - V_\odot \sin l \sin b + W_\odot \cos b). \quad (A3)$$

The reason we do the correction this way round (rather than simply in (U, V, W)) is because we wish to see how the line-of-sight velocities and proper motions are constituted. For example, the Sun is moving up towards the Galactic pole. To correct for this in the line-of-sight velocity when looking above and below the plane this contribution from $W_\odot$ is subtracted and added, respectively. Hence, the solar motion must be corrected for before examining trends in V_{los}, especially if averaging over positive and negative Z.

The (U, V, W) components are given by

$$U = V'_{\mathrm{los}} \cos l \cos b - V'_l \sin l - V'_b \cos l \sin b, \quad (A4)$$

$$V = V'_{\mathrm{los}} \sin l \cos b + V'_l \cos l - V'_b \sin l \sin b, \quad (A5)$$

$$W = V'_{\mathrm{los}} \sin b + V'_b \cos b, \quad (A6)$$

where U is positive towards the Galactic Centre. For small l, this reduces to

$$U = V'_{\mathrm{los}} \cos b - V'_b \sin b, \quad (A7)$$

$$V = V'_l, \quad (A8)$$

$$W = V'_{\mathrm{los}} \sin b + V'_b \cos b. \quad (A9)$$

Similar results are obtained near $l = 180°$, obviously with some sign changes. To convert to cylindrical coordinates, we first define the Cartesian values corrected for the circular velocity at the solar radius:

$$V_X = U \quad (A10)$$

$$V_Y = V + V_{c,0} \quad (A11)$$

$$V_Z = W, \quad (A12)$$

where we use the nominal value $V_{c,0} = 220 \ \mathrm{km \ s^{-1}}$ in the majority of this paper. The cylindrical components are then

$$V_R = ((X - R_\odot)V_X + YV_Y)/R \quad (A13)$$

$$V_\phi = -((X - R_\odot)V_Y - YV_X)/R \quad (A14)$$

$$V_Z = V_Z, \quad (A15)$$

with $R = \sqrt{(X - R_\odot)^2 + Y^2}$. For the small l (or $l \sim 180°$) discussed in Section 7 where $y \simeq 0$, and for the solar neighbourhood where $X - R_\odot < 0$, these reduce to $V_R \simeq -U$ and $V_\phi \simeq V + V_{c,0}$ and so these values are interchangeable in this regime.

This paper has been typeset from a TEX/LATEX file prepared by the author.